



# **A review of processing of Cu/C base plate composites for interfacial control and improved properties**

Jean-François Silvain, Jean-Marc Heintz, Amélie Veillere, Loïc Constantin,  
Yong Feng Lu

## **► To cite this version:**

Jean-François Silvain, Jean-Marc Heintz, Amélie Veillere, Loïc Constantin, Yong Feng Lu. A review of processing of Cu/C base plate composites for interfacial control and improved properties. International Journal of Extreme Manufacturing, 2020, 2 (1), 012002 (21 p.). 10.1088/2631-7990/ab61c5 . hal-02490011

**HAL Id: hal-02490011**

**<https://hal.science/hal-02490011>**

Submitted on 8 Jul 2020

**HAL** is a multi-disciplinary open access archive for the deposit and dissemination of scientific research documents, whether they are published or not. The documents may come from teaching and research institutions in France or abroad, or from public or private research centers.

L'archive ouverte pluridisciplinaire **HAL**, est destinée au dépôt et à la diffusion de documents scientifiques de niveau recherche, publiés ou non, émanant des établissements d'enseignement et de recherche français ou étrangers, des laboratoires publics ou privés.

TOPICAL REVIEW • OPEN ACCESS

## A review of processing of Cu/C base plate composites for interfacial control and improved properties

To cite this article: Jean-François Silvain *et al* 2020 *Int. J. Extrem. Manuf.* **2** 012002

View the [article online](#) for updates and enhancements.

## Topical Review

# A review of processing of Cu/C base plate composites for interfacial control and improved properties

Jean-François Silvain<sup>1,2,3</sup> , Jean-Marc Heintz<sup>1</sup>, Amélie Veillere<sup>1</sup>,  
Loïc Constantin<sup>1,2</sup> and Yong Feng Lu<sup>2,3</sup>

<sup>1</sup> Univ. Bordeaux, CNRS, Bordeaux INP, ICMCB, UMR 5026, F-33600 Pessac, France

<sup>2</sup> Department of Electrical and Computer Engineering, University of Nebraska-Lincoln, Lincoln, NE, 68588, United States of America

E-mail: [jean-francois.silvain@icmcb.cnrs.fr](mailto:jean-francois.silvain@icmcb.cnrs.fr) and [ylu2@unl.edu](mailto:ylu2@unl.edu)

Received 14 October 2019, revised 4 December 2019

Accepted for publication 13 December 2019

Published 29 January 2020



## Abstract

The increase in both power and packing densities in power electronic devices has led to an increase in the market demand for effective heat-dissipating materials with a high thermal conductivity and thermal expansion coefficient compatible with chip materials while still ensuring the reliability of the power modules. Metal matrix composites, especially copper matrix composites, containing carbon fibers, carbon nanofibers, or diamond are considered very promising as the next generation of thermal-management materials in power electronic packages. These composites exhibit enhanced thermal properties, as compared to pure copper, combined with lower density. This paper presents powder metallurgy and hot uniaxial pressing fabrication techniques for copper/carbon composite materials which promise to be efficient heat-dissipation materials for power electronic modules. Thermal analyses clearly indicate that interfacial treatments are required in these composites to achieve high thermal and thermomechanical properties. Control of interfaces (through a novel reinforcement surface treatment, the addition of a carbide-forming element inside the copper powders, and processing methods), when selected carefully and processed properly, will form the right chemical/mechanical bonding between copper and carbon, enhancing all of the desired thermal and thermomechanical properties while minimizing the deleterious effects. This paper outlines a variety of methods and interfacial materials that achieve these goals.

**Keywords:** metal matrix composite, physical properties, interface/interphase, copper, carbon reinforcement

## 1. Introduction

Electronic packaging refers to the providing of service and safety devices that enable continued and efficient operation of

electronic components. Electronic components typically refer to assemblage of resistors, capacitors, transistors, diodes, etc, in a complex well-designed group as integrated circuits usually soldered to a printed circuit board. Since these components are very sensitive in all respects, the packaging is designed to prevent damage, avoid exposure to dirt and other adverse environment, dissipate heat very efficiently, enhance reliable service life and sustain efficient working conditions. The industry is involved in an endless search of new materials that enable electronic systems with ever-increasing density of components, through higher heat dissipation capability, lower

<sup>3</sup> Authors to whom any correspondence should be addressed.



Original content from this work may be used under the terms of the [Creative Commons Attribution 3.0 licence](https://creativecommons.org/licenses/by/3.0/). Any further distribution of this work must maintain attribution to the author(s) and the title of the work, journal citation and DOI.

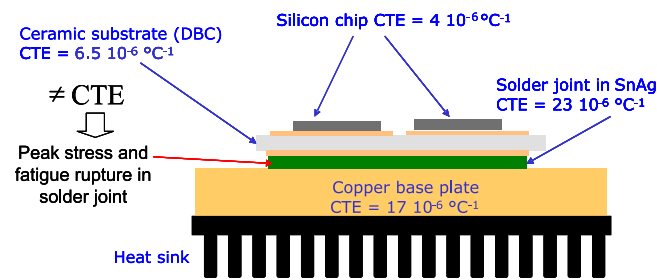


**Figure 1.** Schematic of a classical microelectronic device with peak stress in the solder joint [1–4].

density, and higher reliability. Figure 1 shows a schematic of a modern electronic device [1–4]. The silicon (Si) chip represents the electronic component where the heat is produced, and this chip needs to be maintained in a stress-free condition with a temperature below 100 °C. When a chip is made of Si carbide, a temperature of up to 250 °C is acceptable. To avoid any stress, materials in contact with the chip should have a coefficient of thermal expansion (CTE) close to  $4 \cdot 10^{-6} \text{ K}^{-1}$ , that of Si. As shown in figure 1, direct bonded copper (DBC: copper–aluminum oxide–copper (Cu– $\text{Al}_2\text{O}_3$ –Cu)), which has a CTE of  $7 \cdot 10^{-6} \text{ K}^{-1}$ , is in contact with the chip. DBC provides good electrical insulation and good heat-spreading characteristics that closely match the CTE of the chip. However, when using alumina, the thermal conductivity (TC) in the critical normal direction is only on the order of  $30 \text{ W m}^{-1} \text{ K}^{-1}$ . The next critical component in the heat-flow chain is the base plate itself, which is the subject of this paper. Table 1 shows the key properties of the CTE, TC ( $k$ ), and density ( $\rho$ ) of various base plate and heat-sink materials [1, 5–9].

Composite materials show the highest potential for application in base plates for electronic applications. They can combine metal, polymer, and ceramics in a broad range of different products and can be tailored to the final desired properties. It is critically important to note that the final properties of composites depend not only on the basic constituent materials but also on the methods of fabrication. Among the large number of different composites, the most efficient and the most commonly developed for heat dissipation purposes are metal matrix composites (MMCs). More specifically, there is great interest in MMCs based on copper (Cu) and aluminum (Al) matrices with a broad range of different reinforcements [6–14]. They show several improvements over current electronic packaging materials, including:

- Lower and tailorable CTE (the higher the volume fraction of reinforcement used, the lower the CTE).
- High heat dissipation capability.
- Lightweight and suitable for aeronautics applications.
- High stiffness at elevated temperatures (for dimensional stabilities at elevated temperatures).

Most of the Cu- or Al-based composites are reinforced by ceramics (particles, short fibers, and long fibers) in order to reduce their high CTE in an effort to match that of the semiconductor or other ceramic substrates. Since carbon reinforcements have both high thermal and electrical

conductivity (table 2), MMCs reinforced with C in its different forms (carbon fibers (CF), carbon nanofibers (CNF), carbon nanotubes (CNT), diamond (D), ...) are composite materials that can present both good TC and low CTE.

Once the composition of both the matrix and the reinforcements is defined, another factor should be considered: the interfaces and interphases. MMCs often use interphases to enhance mechanical adhesion and tailor the overall properties of the resultant matrix. The formation of interphases is particularly crucial in composites comprised of chemically and thermo-mechanically dissimilar compositions [9, 13, 16]. Interfaces/phases play a key role in the final properties of a composite because they allow the transfer of properties between the matrix and the reinforcement. In MMCs, two kinds of systems are considered:

- Reactive systems: existing reaction between the matrix and the reinforcement.
- Nonreactive systems: chemical inertia between the matrix and the reinforcement.

Reactive systems are those in which there is a chemical instability between the matrix and the reinforcement, i.e. there is a formation of an interphase. This interphase can damage the reinforcement and decrease the final properties of the composite. For example, in a composite material with an Al matrix reinforced by carbon fibers (Al/CF), the formation of an aluminum carbide ( $\text{Al}_4\text{C}_3$ ) interphase damages the fiber and creates porosities at the interface, which decreases the global properties of the composite material.

Nonreactive systems are those in which there is little or no chemical interaction between the matrix and the reinforcement. In this case, a mechanical clamping of the matrix on the reinforcement occurs from a CTE mismatch that results in thermal residual stress during cooling. To optimize this kind of composite, an increase in the reactivity between the matrix and the reinforcement is needed to create a strong chemical bond at the interface. For example, in a composite material with a Cu matrix reinforced by carbon fibers (Cu/CF), there is a chemical inertia between the Cu and C. Some doping elements are then added, either in the matrix or onto the CFs, to improve the formation of a controlled interphase between the CFs and the Cu matrix [16–26].

Several processes have been developed to elaborate upon copper/carbon composites (Cu/C). They are based either on the passage through a liquid phase (Cu melting) or on a solid-state heat treatment. The squeeze casting [27, 28] is likely one of the most usual manufacturing processes for elaboration of MMC. This process consists in the production of rigid porous structures with reinforcement that are further infiltrated by copper molten under pressure. The main inconvenient of this technique is to keep steady the liquid metal during the infiltration step because of the high melting point of copper (1083 °C). Another inconvenience is related to low wettability of copper with carbon, which involves a high infiltration pressure. Also, this low wettability can lead to reinforcement agglomerates and the presence of micro porosity in composites. So, the squeeze casting is not the best processing route for the elaboration of Cu/C composites. The alternative

**Table 1.** Key properties of base-plate materials [1, 5–9].

Matrix		Reinforcement type (vol.%)		Density (g cm <sup>−3</sup> )	CTE (10 <sup>−6</sup> K <sup>−1</sup> )	Thermal conductivity (W m <sup>−1</sup> K <sup>−1</sup> )
METALS						
W/Cu	90/10	—	0	17.2	6.5	202
	85/15	—	0	16.6	7.1	211
	80/20	—	0	16.4	7.6	215
Mo/Cu	85/15	—	0	10	7.0	160
	80/20	—	0	9.9	8.0	170
Al/Si	70/30	—	0	2.3	7.0	120
	60/40	—	0	2.4	9.0	129
W/Ni/Cu	90/6/4	—	0	17.0	5.5	120
	95/3.5/1.5	—	0	18.0	4.5	173
Cu/Invar/Cu	—	—	0	8.3	6.5	138 (X–Y); 40 (Z)
Cu/Mo/Cu	—	—	0	9.8	6.0	210 (X–Y); 170 (Z)
Al	—	—	0	2.7	23	237
Cu	—	—	0	8.96	17	401
Ag	—	—	0	10.5	19.1	420
COMPOSITES						
Carbon	VGCF	39	1.8–2	—		736
Epoxy	C fiber	60	1.85	−1.1		310 (X–Y)
Epoxy	VGCF	73	1.87	—		661
Cu	Diamond	50	5.35	5.5		420
Cu	C fiber	28	7.2	6.5		290 (X–Y)
Cu	VGCF	50	6.5	5.5		840
Cu	C particles	40	5.9	9–10		150–300
Al	C fiber (long)	65	2.11	8		158 (X–Y)
Al	VGCF	37	2.44	5		642
Al	C fiber (short)	30	2.46	7.5		200
Al	C fiber (short)	40	2.40	4.0		230
Al	B fiber	20	2.6	12.7		180
Al	SiCp	55	2.9	10.3		180
Al	SiCp	60	2.9	9–10		180
Al	Graphite	50–70	2.2–2.0	6.5–9.5		190–270

**Table 2.** Properties of different kinds of reinforcements used in base-plate applications [6, 15].

Reinforcements	Average diameter ( $\mu\text{m}$ )	Density ( $\text{g cm}^{-3}$ )	Thermal conductivity ( $\text{W m}^{-1} \text{ K}^{-1}$ )	CTE ( $10^{-6} \text{ K}^{-1}$ )	Price ( $\text{€ kg}^{-1}$ )
SiC	30–300	3.2	200–300	4.5	50–200
Carbon fiber (CF)	10	2.0–2.2	100–900	–1.0	30–400
Carbon nanofiber (CNF)	0.1–0.2	2.0	1000–1200	–1.0	500–1000
Carbon nanotube (CNT)	0.001–0.01	2.0	3000–6000	–1.0	10–100 000
Diamond (D)	20–600	3.1	1500–3000	1.0	200–2000

processing method is the powder metallurgy route, i.e. the powder of metal matrix is mixed to the reinforcements and this mixture is then sintered in solid state. There are various powder metallurgy processes that can be distinguished by the nature and the form of the physical constraints applied on the granular compact (temperature, pressure, ...). Conventional powder metallurgy process usually does not imply any pressure, which does not allow high final densities to be obtained for composites, particularly in the case of high-volume fraction of reinforcements. Therefore, an external pressure is very

often applied on the powder mixture during the sintering step to favor the densification of MMC. Uniaxial hot pressing (HP), hot isostatic pressure, spark plasma sintering (SPS), etc., are different techniques that refer to HP processes that are mainly used to prepare MMC and especially Cu/C composite materials [29].

In past years, the literature on Cu/C composite materials for power electronics has expanded significantly. Emphasis has been put either on the nature of carbon reinforcement, with the use of CNT, graphene or diamond for example

[30–38], or on the process itself with many articles on the use of SPS [39–41]. In addition, the critical role of the nature of interfaces/interphases has also been the subject of many developments. However, to our knowledge, there is no general review of the various strategies that can be designed and proposed to promote the formation of controlled interfaces/interphases in such a nonreactive system, i.e. copper/carbon, in relation to the fabrication process. So, we present in this paper an extensive review of the different approaches to process Cu/C composite materials (the C reinforcement being CF, CNF or D) using one of the simplest preparation methods, i.e. powder metallurgy and with a control of interfaces.

We begin with a description of the solid-state sintering process that we used to fabricate Cu/C composite materials. We show how the absence of an interface between the matrix and reinforcement limits thermal properties, especially in terms of thermal fatigue under cycling stresses. Then we address the formation of controlled chemical interphases during solid-state sintering using either a change in the composition of the matrix or the coating of the C reinforcements. The second part of the paper is devoted to describing the liquid phase sintering of Cu/C composites and how it improves control of interphases and thermal properties. Lastly, the tape casting method is presented for use when composite layers are needed.

## 2. Experimental section

### 2.1. Characterization methods for microstructure and chemical analyses

**2.1.1. Scanning electron microscopy (SEM)/electron probe microanalyses (EPMA).** Scanning electron microscopy (SEM) analysis was performed in two modes (secondary electron (SE) and back-scattered electron (BSE)) with a TESCAN VEGA II from the Eloise France Company working at 10 and 20 kV with a current beam of 90  $\mu$ A. The bulk samples were investigated by electron probe microanalyses (EPMA) with metallic ( $K\alpha$ ) standards.

**2.1.2. Transmission electron microscopy (TEM).** Transmission electron microscopy (TEM) micrographs were done using a JEOL JEM-2100 microscope working at 200 kV and equipped with energy-dispersive x-ray spectroscopy (EDS).

**2.1.3. X-ray photoelectron spectroscopy (XPS).** X-ray photoelectron spectroscopy (XPS) was used to investigate the chemical composition of the surface of C reinforcements. The XPS measurements were undertaken using a VG ESCALAB 220-iXL instrument, with a monochromatic Al  $K\alpha$  radiation source. In all cases, the spectra were charge

referenced to hydrocarbon contamination C 1s peak at a binding energy of 284.5 eV.

### 2.2. Characterization of physical properties

**2.2.1. Measurement of density.** The theoretical density of the composites was calculated using the rule of mixture given below:

$$\rho_c = \rho_m V_m + \rho_r V_r,$$

where  $\rho_m$ ,  $\rho_r$ , and  $V_m$ ,  $V_r$  are the densities and the volume fractions of the matrix and reinforcement, respectively. Due to the low number of additives which are used in some cases, their contribution was neglected or considered in the error bars. Experimental measurements were carried out using the Archimedes' method.

**2.2.2. Thermal conductivity.** TC  $k$  of a material indicates the ability of a material to conduct heat and is measured in terms of watts per kelvin per meter, where  $k$  is given by

$$k = \frac{1}{A} \frac{dQ}{dt} \frac{dx}{dT}$$

and  $k$  can be thought of as the heat flux  $\frac{dQ}{dt}$  divided by the temperature gradient  $\frac{dT}{dx}$  on the cross-sectional area  $A$  of the conductive surface. The physics of how heat is conducted in a medium are quite different for a metal (e.g. Cu or Al) compared to that of ceramics (e.g. alumina). In metals, the TCs occur as free-moving electrons transfer heat and current when subjected to temperature or voltage differential. However, in ceramics, the heat transfer predominantly occurs through the elastic vibrations of the lattice, the so-called phonon modes. Thermal phonon wave propagation is represented by the superposition of longitudinal (acoustic) and transverse (optical) phonons.

The thermal diffusivity (TD) ( $\alpha$ ) can be measured using a flash laser technique (Netzsch LFA 457 MicroFlash<sup>®</sup>). In this technique, a pulse laser excites the top surface of the sample; and the variation in temperature is measured in the opposite face using an indium antimonide (InSb) infrared detector. The measurement is usually done on samples 6 mm in diameter and between 2 and 5 mm in thickness. The faces must be parallel in order to obtain accurate and reproducible results. Before the experiment, the sample is covered with a thin film of graphite in order to avoid radiation. The TC ( $k$ ) of the material is deduced from the formula:

$$k = C_p \times \rho \times \alpha,$$

where  $\rho$  corresponds to the density of the composite measured by the Archimedes' method, and  $C_p$  is the specific heat calculated with a rule of mixture.

**2.2.3. Measurement of CTE.** When the temperature of a material is raised, the material undergoes an expansion leading to new linear and volumetric dimensions. These expansions are then quantified as linear ( $\alpha$ ) and volumetric



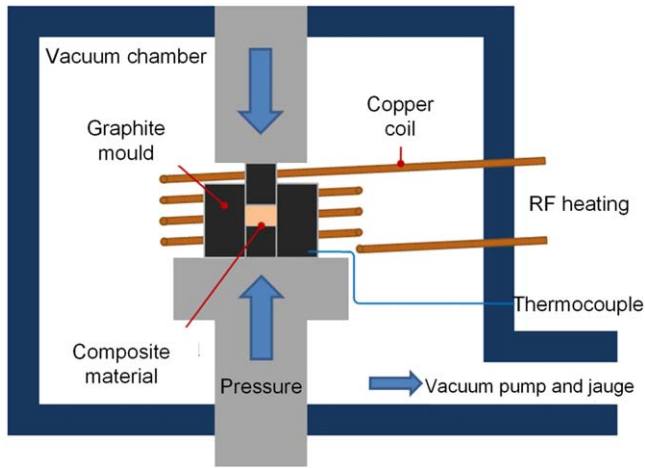


**Figure 2.** Schematic of a hot press system. Reproduced with permission from [56].

( $\alpha_V$ ), respectively, such that

$$\alpha = \frac{1}{l} \left[ \frac{dl}{dT} \right]_P \text{ and } \alpha_V = \frac{1}{V} \left[ \frac{dV}{dT} \right]_P,$$

where  $\alpha$  and  $\alpha_V$  are both functions of temperature,  $l$  is the instantaneous length,  $T$  is the temperature,  $V$  is the volume, and the differential is evaluated at constant pressure  $P$ . For all practical purposes, both  $l$  and  $V$  are measured on finite dimensioned samples when the temperature of the sample is raised by a finite value  $\Delta T$ . When evaluating the CTE of the composite, the overall external change in dimensions is measured.

The CTE is measured with a differential dilatometer (Netzsch DIL 402 C). In this technique, a sample with a known initial length ( $l$ ) is heated; and the variation in length is measured during thermal cycling. In our experiment, the heating rate was  $2^\circ\text{C min}^{-1}$  and ranged from room temperature to  $250^\circ\text{C}$ . A curve of  $\Delta l/l$  with the temperature was plotted, and the measured slope gave the value of the CTE. Before the measurement, the procedure was standardized using an alumina sample, accounting for the dilatation of the sample holder, pusher, and other components of the dilatometer.

### 3. Results and discussion

#### 3.1. Base-plate composites fabricated using solid-state sintering

Most of the composite materials prepared in these studies were sintered using uniaxial HP. The applied pressure helps the densification process, especially when a high-volume fraction of C is introduced. The hot-pressing technique has three degrees of freedom: time, pressure, and temperature. By tuning these parameters, the microstructure of the final material can be adjusted. A schematic of a classical hot-pressing device is shown in figure 2. It combines an induction heating system with a hydraulic pressing jack. The induction-heating technique has the advantage of allowing the material to be

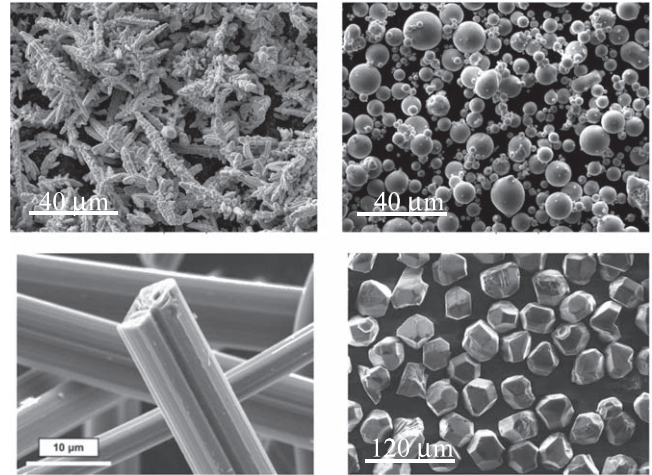


**Figure 3.** Typical powders used for the fabrication of Cu/C composite base plates: (a) dendritic Cu, (b) Cr-allied spherical Cu, (c) C fiber, and (d) diamond.

heated without any direct contact with the heat source. HP also has the advantages of being a fast, low cost, and low energy consumption sintering technique, relative to other processes employed to fabricate Cu/C composite materials, such as liquid infiltration, SPS, or pulse plasma sintering [39–55].

Typical powders that are used for fabricating composite base plates are presented in figure 3. Different vol.%s of reinforcement were considered, from 10 to 50 vol.%. Copper and C powders were first mechanically mixed using TURBULA® 3D or an acoustic mixer (Resodyn) and then uniaxially hot pressed for 20 to 30 min, under vacuum ( $10^{-1}$  mbar) or argon/hydrogen (Ar/H<sub>2</sub>) 5 vol.% atmosphere. The sintering temperature was fixed at  $650^\circ\text{C}$ , and the effective applied pressure on the pistons was 50 MPa when Cu dendritic powders were involved. When spherical powders were used, the pellets were hot pressed using a graphite mold and graphite pistons, which were induction heated between  $850^\circ\text{C}$  and  $950^\circ\text{C}$ . After HP, the CFs are randomly oriented in a plane perpendicular to the pressure direction.

**3.1.1. No interface between matrix and reinforcement.** As explained in the introduction, the system investigated was Cu/C due to its high potential thermal performance. From a chemical point of view, there is almost no mutual solubility of these two elements. The Cu–C phase diagram (figure 4) shows that the C solubility into Cu was less than  $4.10^{-4}$ , with this value obtained only at a high temperature ( $1000^\circ\text{C}$ ). This means that the sintering of a mixture of Cu powder and C reinforcements (fiber, diamond, ...) will give rise to a composite with pure interfaces between the matrix and the reinforcements.

The densities of the composite materials containing different reinforcement percentages are given in table 3. It can be noted that due to the density of the C species (close to  $2.2\text{ g cm}^{-3}$ ), the global density of the Cu composite materials decreased when the volume fraction of the C reinforcement increased. It has to be noted that for all of these materials, the

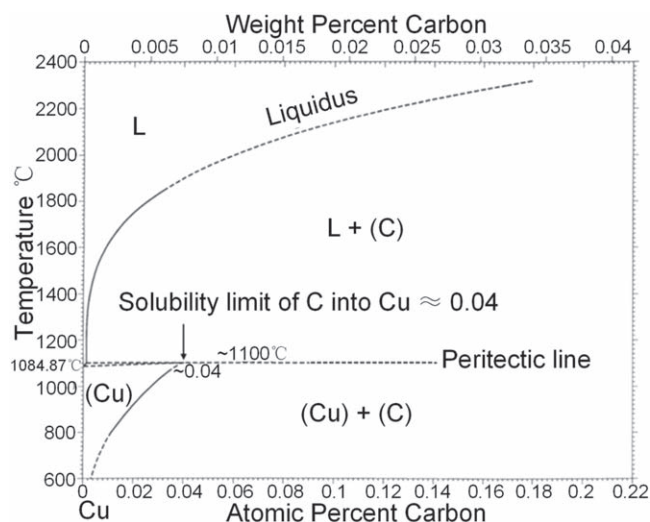


**Figure 4.** Cu–C phase diagram. Reproduced with permission from [57].

percentage of porosities inside the materials was lower than 3% after sintering. Porosities are inherently introduced in these material systems and adversely affect the TC of the composite materials. A clear decrease of TC occurred above 5 vol.%, which corresponds to the presence of interconnected and open pores in the material. The TC values also decreased. The TCs of both XN100 and CN80 carbon fibers in the direction of the CF axis were quite different even if they were the same in the direction perpendicular to this axis (close to  $10 \text{ W m}^{-1} \text{ K}^{-1}$ ). The TC was close to  $900 \text{ W m}^{-1} \text{ K}^{-1}$  for the XN100 and close to  $320 \text{ W m}^{-1} \text{ K}^{-1}$  for the CN80. Table 3 shows that whatever the CF used, the TCs of the composite materials decreased, with respect to pure Cu, when the CF volume fraction increased. Because of the random orientation of the CFs in the planes perpendicular to the pressure direction, the global conductivity of the CFs was smaller than the TC of Cu leading to a TC of the Cu/CF composite materials smaller than pure Cu. However, due to the fact that the TC of the XN100 CF was larger than the TC of the CN80, the global TC of the Cu/CF (XN100) was larger than the TC of the Cu/CF (CN80). In addition, the TC of the composite materials in the perpendicular direction was much smaller than in the parallel one because of the orientation of the CF (perpendicular to the pressure direction) and the low TC of the CF through the perpendicular direction ( $10 \text{ W m}^{-1} \text{ K}^{-1}$ ).

The TCs of the Cu/D materials were obviously isotropic due to the isotropic properties of the D particles. In opposition to the CF behavior, as the TC of D was larger than Cu, the TCs of the Cu/D materials increased with the diamond volume fraction and the size (linked to their TCs) of the D particle.

For the Cu/CF composite, the CTE values did not change with the quality of the CFs, just with their volume fraction. The CTE, measured in the parallel direction, decreased when the CF volume fraction increased. The larger CTE measured for the D reinforcement was linked with the larger CTE of the D particle with respect to the CFs.

The evolution of the TCs of different Cu/D (with and without an interfacial zone) with the number of thermal cycles

( $-40^\circ\text{C}$ ,  $+150^\circ\text{C}$  with a positive and negative ramp of  $10^\circ\text{C min}^{-1}$  and a holding time of 30 min at both high and low temperature) is plotted in figure 5. This graph clearly shows that the presence of chemical reaction zone at the Cu–C interface has a positive effect on TC evolution with the number of thermal cycles. Large degradation was measured after 500 cycles for the Cu/D materials free of an interfacial zone, whereas for both Cu/coated D and chromium (Cr) carbide, the interface shows a global TC stability.

Powder metallurgy is a convenient and simple method of processing Cu/C composites. The thermal properties depend on the performance of both the C reinforcements and the final density of the composite material. However, the absence of chemical bonds between the reinforcement and matrix prevents good thermal behavior from being obtained when the composite material is thermally cycled.

### 3.1.2. Chemical interface (or interphase) between matrix and reinforcement

**3.1.2.1. Change of the composition of the matrix.** The idea for this approach consists in introducing an alloying element in the Cu matrix that will preferentially react with the C reinforcement during the processing of the composite. Therefore, it will lead to the formation of strong chemical bonds (carbide compound) at the interface between the matrix and reinforcement.

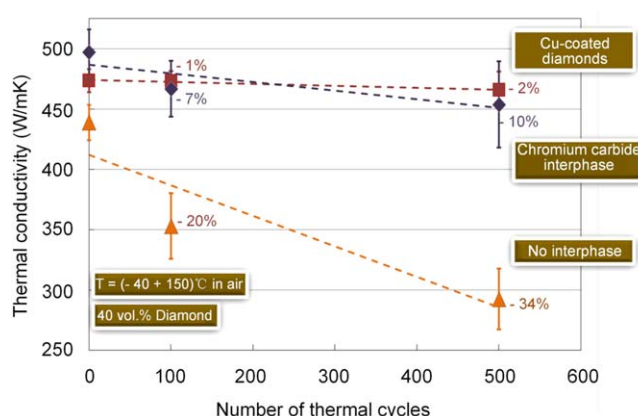
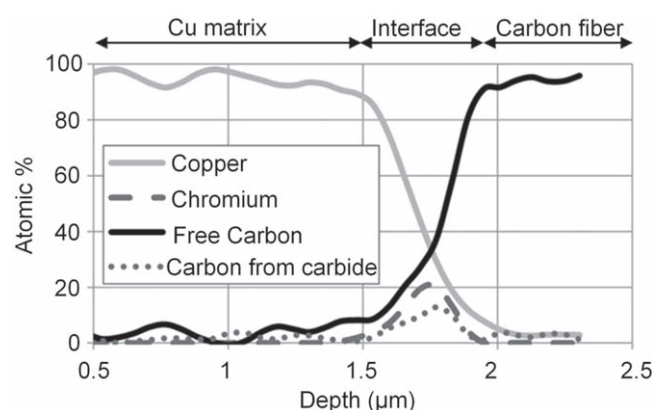
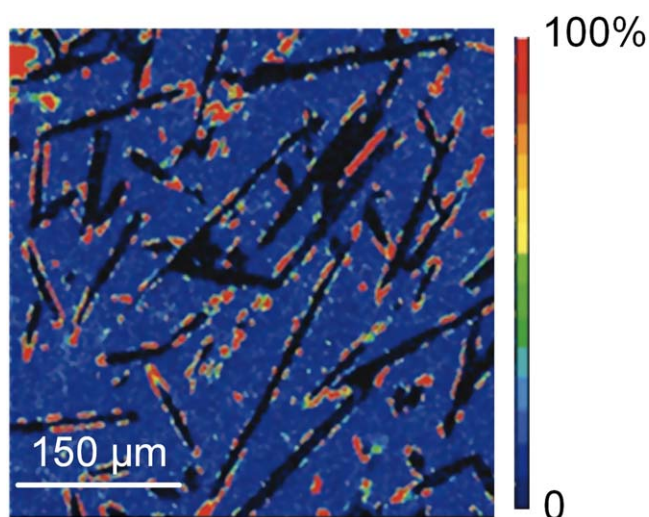
**3.1.2.2. Cu(Cr/B)/CF.** The first systems that were investigated were copper–chromium (Cr) and copper–boron (B) alloys [40]. These systems have been chosen due to the fact that these two elements (Cr and B) tend to react with carbon to create a chemical interface (carbide forming additive) between the matrix and the reinforcement. The amounts of B and Cr were chosen in order to have the alloying element in a solid solution in Cu and prevent the formation of particles inside the matrix, which can decrease the thermal properties. The C reinforcements were chopped CFs ( $\varnothing \sim 10 \mu\text{m}$ , lengths ranging between 100 and  $400 \mu\text{m}$ ). The composite materials were prepared according to the classical powder metallurgy method previously described: uniaxial hot pressed at  $950^\circ\text{C}$  under 50 MPa for 20 min under  $\text{Ar}/\text{H}_2$  (5 vol.%). Dense composites were obtained ( $d_{\text{rel}} \sim 96\% d_{\text{th}}$ ). An optimized annealing treatment was then performed ( $1000^\circ\text{C}$ , 24 h, under reducing atmosphere) to increase the diffusion of the alloying element (Cr) toward the Cu–CF interface and, therefore, create stronger carbide interface bonds.

Figure 6 presents the Cr EPMA map of a Cu–Cr/CF composite material. As can be observed, the Cu matrix is almost free of Cr, which has diffused toward the Cu–C interface. A representative Auger electron spectroscopy (AES) line profile is shown in figure 7. The figure shows three distinct zones: the matrix, the interphase, and the fiber. Both Cr and C are present only in the interphase. This analysis confirmed the segregation of Cr in the form of Cr carbide at the Cu–CF interface. The thickness of the interphase ranged between 0.1 and  $1 \mu\text{m}$ .



**Table 3.** Measured values of the density ( $\text{g cm}^{-3}$ ), CTE ( $10^{-6} \text{ K}^{-1}$ ) and TC ( $\text{W m}^{-1} \text{ K}^{-1}$ ), with the CF (D) volume fraction, for different Cu/CF (Cu/D) composite materials ( $\Phi$  is the diameter of the diamond powders).

CF vol. %	Density	CTE	TC	Parallel TC		Perpendicular TC	
				XN100	CN80	XN100	CN80
0	8.96	17	—	400	400	400	400
10	8.24	16	—	380	355	320	320
20	7.53	14	—	360	320	255	255
30	6.81	11	—	340	280	180	180
40	6.10	8	—	310	250	160	160
D vol. %							
40 ( $\Phi = 60 \mu\text{m}$ )	6.78	12	500	—	—	—	—
40 ( $\Phi = 240 \mu\text{m}$ )	6.78	12	650	—	—	—	—

**Figure 5.** Evolution of thermal conductivity of different Cu/C composites during thermal cycling. Reproduced with permission from [56].**Figure 7.** AES depth profile through Cu–Cr/CF interface after annealed treatment. Reprinted from [58], Copyright 2011, with permission from Elsevier.**Figure 6.** EPMA mapping of Cr in Cu–Cr/CF composite materials. Reprinted from [58], Copyright 2011, with permission from Elsevier.

TEM studies were performed on both Cu–Cr/CF and Cu–B/CF composite materials in order to analyze the interface at a nanometric scale and determine its crystallographic structure (figure 8). Three zones were visible (figures 8(a) and (b)) and the electronic diffraction analysis of each zone (figure 8(c)) showed,

respectively, the crystallographic structures of the Cu matrix, the CF, and the interfacial zone composed of chromium carbide ( $\text{Cr}_3\text{C}_2$ ) (Pnma space group). The diffraction pattern acquired in the Cu matrix showed the presence of metallic Cu with no trace of an alloying element in the cluster shape. Therefore, if an alloying element was present in the matrix, it would be in a small amount and as a solid solution in Cu.

TD was measured along the pressure direction of the densification process due to technical limitations during the experiments. Due to the anisotropic microstructure in the samples with a preferential orientation of the CF perpendicular to the pressure axis, the measurement corresponds to the TD perpendicular to the fiber axis. Due to the low transverse TC of the fiber ( $5 \text{ W m}^{-1} \text{ K}^{-1}$ ), it should be noted that the lowest TD of the composite material was measured. Measures were taken for both Cu–Cr/CF and Cu–B/CF composites. The calculated TCs from the experimental TDs are given in table 4. Indeed, the Cu alloy matrices (Cu–Cr and Cu–B) had a lower TC than pure Cu, whereas the final composites had the same TC. This phenomenon can be explained by the diffusion of the alloying element taken for both the Cu–Cr/CF and Cu–B/CF composites at the Cu/CF interfaces which led to the formation of a carbide at the interface and a matrix almost free of an alloying element. This means that the value of the TC depends mostly on the TC of the matrix and reinforcement and not on the interface type (mechanical or

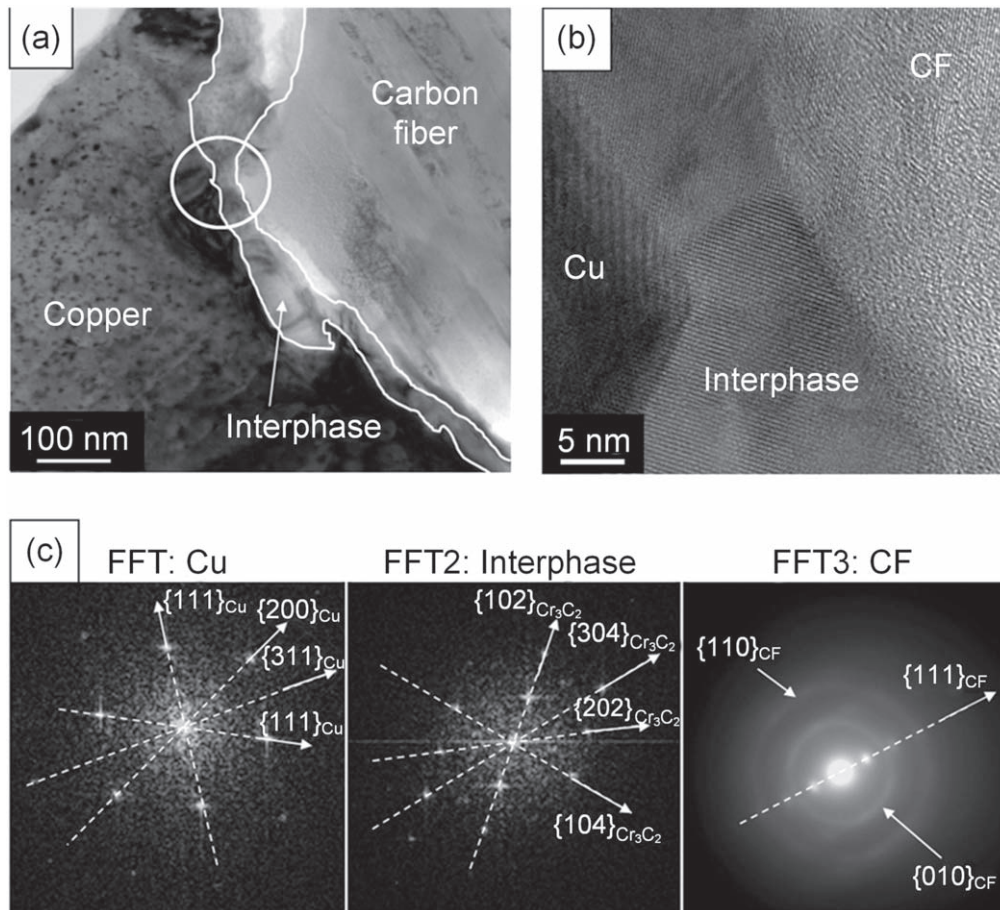


**Figure 8.** TEM micrographs (a) of the Cu–Cr/CF composite material after annealing treatment, (b) magnification of the circled area in (a), and (c) diffraction pattern inside the Cu, the interphase, and the CF. Reprinted from [58], Copyright 2011, with permission from Elsevier.

**Table 4.** Transverse thermal conductivity and parallel CTE of Cu–X/CF composite materials (30 vol.%).

Matrix	Reinforcement	Thermal conductivity (W m <sup>-1</sup> K <sup>-1</sup> )	CTE (10 <sup>-6</sup> K <sup>-1</sup> )
Cu		400	17
	CN80C	180	14
	XN100	220	14
Cu–Cr		360	17
	CN80C	180	12
	XN100	190	14
Cu–B		370	17
	CN80C	180	12
	XN100	230	13

chemical). Raman spectroscopy analyses of CN80C and XN100 fibers gave values of  $I_G/I_D$  of 4.5 and 7.3, respectively. These ratios confirmed the higher quantity of crystalline defects on the CN80C fiber; therefore, this type of CF was more reactive if we assume that the defects were linked to the nucleation sites for carbide formation. Finally, stronger chemical interfaces were present between the Cu alloy matrices and CN80C CF than with XN100 CF. These stronger chemical links can be associated with higher transfer properties resulting in lower measured CTE.

Whatever the matrix used (pure Cu or Cu alloys), the addition of CFs inside the matrix led to a decrease of the CTE of the composite material. For Cu–X/CF composites, with Cu–Cr or Cu–B matrices, an improvement of the CTE compared to the Cu/CF reference composite was measured. The annealing treatment was advantageous because it led to the full diffusion of the alloying element toward the interfacial zone and the formation of a stronger carbide chemical bond ( $\text{Cr}_3\text{C}_2$ ) at the Cu/CF interface. This Cr carbide interphase preserved the contact between the matrix and the reinforcement and avoided delamination of the material, which resulted in a decrease of the composite material CTE. These thermomechanical analyses showed that the addition of an alloying element (Cr) produced TC equivalent to Cu/CF composites but with a CTE improvement of 25%.

The chemical and microstructural characterizations of the Cu–X/CF composite materials showed diffusion of the alloying element ( $X = \text{Cr}$  or  $\text{B}$ ) in the Cu matrix toward the Cu–CF interface. Analyses at a nanometric scale clearly identified the crystalline structure of the interfacial zone, i.e.  $\text{Cr}_3\text{C}_2$  for the Cu–Cr/CF composites and boron carbide ( $\text{B}_4\text{C}$ ) for the Cu–B/CF. Measurements of thermomechanical properties for each composite demonstrated the influence of the interfacial zone composition and the reinforcement type on the material properties. We produced a promising

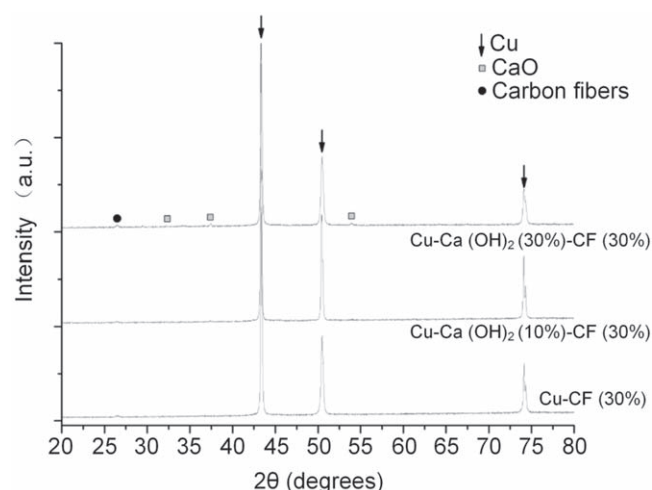


**Figure 9.** X-ray patterns of Cu/CF(30%), Cu(OH)<sub>2</sub>(10%)/CF(30%), and Cu(OH)<sub>2</sub>(30%)/CF(30%) composites. [59] 2014 © Springer Science+Business Media New York. With permission of Springer.

composite by adding Cr in the Cu matrix and using CN80C CFs as reinforcement. Compared to a similar composite material without an alloying element, a 25% improvement to the CTE was measured.

**3.1.2.3. Cu–Ca/CF.** Calcium (Ca) can also be added to Cu/CF (30 vol.%) composites to modify their thermal properties [59]. In fact, because Ca is not stable under air (i.e. the rapid formation of calcium hydroxide (Ca(OH)<sub>2</sub>) is observed), it corresponds to a study of the effects of Ca(OH)<sub>2</sub> on the TC and the CTE of a Cu/CF composite base plate.

Numerous composites with the composition Cu–Ca(OH)<sub>2</sub>*x* (X%)/CF(30 vol.%) were fabricated where *x* = 0 vol.%, 0.5 vol.%, 1 vol.%, 3 vol.%, 5 vol.%, 10 vol.%, and 30 vol.%. For each sample, the sintering conditions led to the required density, above 98%. However, when the content of Ca(OH)<sub>2</sub> increased, the density increased, up to 106%. These too-high values can be explained by the transformation of Ca(OH)<sub>2</sub> in calcium oxide (CaO) that can occur during sintering. Indeed, if the density of CaO (i.e. 3.3 g cm<sup>−3</sup>) were used instead of Ca(OH)<sub>2</sub> (i.e. 2.24 g cm<sup>−3</sup>), the relative density would decrease at 100%. Thus, the fact that this reaction can occur during sintering at 700 °C was considered and was in agreement with the literature [60].

In figure 9, the x-ray patterns are given for *x* = 0, 10, and 30 vol.%. The x-ray pattern of the sample Cu–Ca(OH)<sub>2</sub> (30 vol.%)–CF(30 vol.%) exhibited some new peaks, which can be indexed by CaO. Therefore, the transformation of Ca(OH)<sub>2</sub> into CaO during the process was confirmed. Moreover, for each composition, the peaks of Cu were fixed. There was no variation in the lattice parameters. Consequently, the Ca did not make a solid solution with the Cu, which agreed with the binary diagram. No porosity was visible at the interface between the Cu and the CFs. These observations are in good agreement with the relative density measured for each sample. The Ca(OH)<sub>2</sub> decomposed in CaO was mainly embedded in the Cu matrix. The size of the CaO precipitates was around 10 to 15 micrometers. The size of the

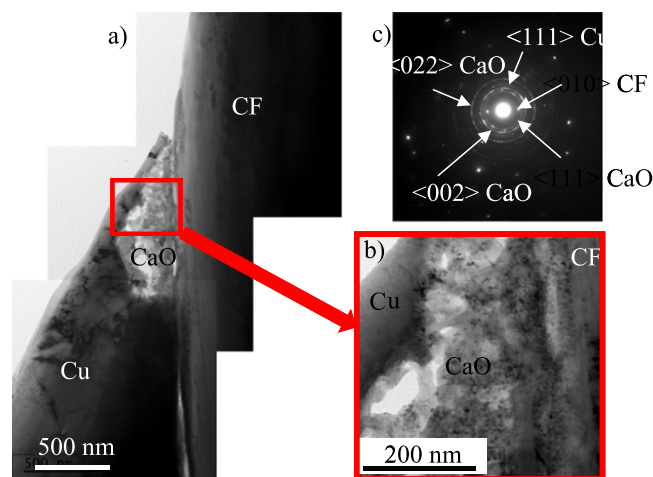


**Figure 10.** TEM micrographs of the Cu–Ca(OH)<sub>2</sub>(3%)/CF(30%) interfacial zone. [59] 2014 © Springer Science+Business Media New York. With permission of Springer.

precipitates remained the same regardless of the amount of CaO, but their number increased when this amount increased. Indeed, according to the literature, the formation of CaC<sub>2</sub> from CaO seems possible above 1000 °C. Thus, at a 700 °C sintering temperature, carbide should not be formed during the process. However, higher temperatures, inside the bulk material, can be locally generated due to the decomposition of Ca(OH)<sub>2</sub>.

The sample with 3 vol.% of CaO was investigated by TEM analysis. The micrographs and the electron diffraction pattern are provided in figure 10. An EDS analysis confirmed the presence of Ca (gray phase on the micrograph) at the interface between the Cu and the CFs. This interphase, where the Ca is located, seems granulous and composed of nanometric particles (figure 10(b)). This nanostructuration was probably induced by the decomposition of Ca(OH)<sub>2</sub>. Ghosh-Dastidar *et al* [61] reported similar behaviors. They explained that during sintering, one grain of Ca(OH)<sub>2</sub> was progressively decomposed in small particles of CaO from the edge to the core. The electron diffraction pattern (figure 10(c)) can be indexed using the crystallographic planes of Cu, C, and CaO. This observation confirmed the transformation of Ca(OH)<sub>2</sub> to CaO. No carbide was found in the numerous electron diffraction patterns studied. However, thin calcium carbide (CaC<sub>2</sub>) may be present at the Ca–CF interphase which cannot be detected by the conventional electron diffraction.

The TC properties and the CTE were measured for each sample. The results are given in figure 11. The composite without Ca(OH)<sub>2</sub>, sintered with the same conditions as the composite with Ca(OH)<sub>2</sub>, exhibited a parallel TC of 303 W m<sup>−1</sup> K<sup>−1</sup>, a perpendicular TC of 202 W m<sup>−1</sup> K<sup>−1</sup>, and a parallel CTE of 11.6 10<sup>−6</sup> K<sup>−1</sup>. These values are slightly higher than the ones from the literature and are used as reference values in this paper [15–17]. For the samples with a low content of Ca(OH)<sub>2</sub> (i.e. ≤1%), the parallel TC did not change; but the perpendicular TC decreased about 5% for *x* = 1% of Ca(OH)<sub>2</sub>. For *x* = 3%, an improvement of around 7% of the parallel TC was measured. In the same way, a



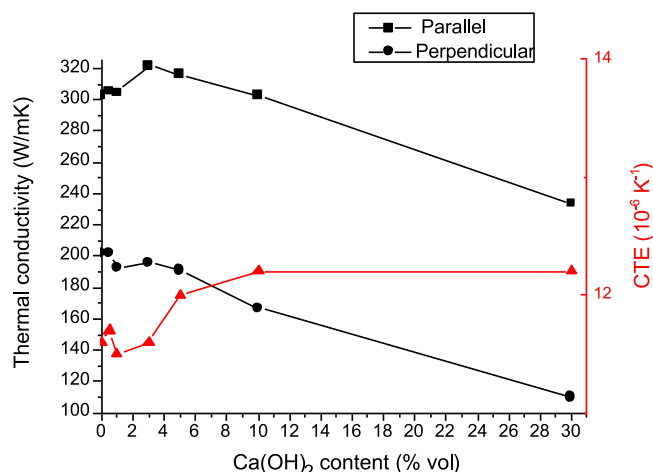


**Figure 11.** TC (circle and square) and CTE (triangle) of the composite Cu–Ca(OH)<sub>2</sub>(X%)/CF(30%) (with  $X = 0, 0.5, 1, 3, 5, 10, 30$ ). [59] 2014 © Springer Science+Business New York. With permission of Springer.

higher or similar TC was measured for  $x = 5$  vol.% and  $x = 10$  vol.%. This improvement remains unexplained. Indeed, CaO material exhibited a low TC value (i.e.  $20 \text{ W m}^{-1} \text{ K}^{-1}$ ). The reasons why the TC increased while a fraction of CaO increased are still unknown. The nanostructuring of CaO from the decomposition of Ca(OH)<sub>2</sub> could be one of the reasons. However, when the content of Ca(OH)<sub>2</sub> increased, the perpendicular TC decreased. The CTE was almost the same for all of the composite materials. Thus, we can suppose that the addition of hydroxide plays no role in thermal expansion. A variation in the CTE can be directly correlated to a change of the interface [62]. Consequently, the Ca(OH)<sub>2</sub> (or CaO) did not change the interface properties between the metallic matrix and the CF. To conclude, the addition of 3% of Ca(OH)<sub>2</sub> led to an improvement in the parallel TC of 7% without affecting the interface between the matrix and fibers. We can suppose that chemical interactions at the interface could both decrease the CTE and maintain a good TC.

**3.1.2.4. Modification of the reinforcement.** The second approach that can be used to tailor interfaces in base plate composites is related to modification of the surface of the reinforcements in such a way that these C reinforcements will be chemically reactive with the Cu matrix during the sintering process. Copper/carbon composites were prepared using the classical powder metallurgy process. However, the reinforcements were pretreated before being mixed with the proper amount of Cu particles and sintered. Four different deposition process routes onto C reinforcements are discussed.

**3.1.3. Salt decomposition route.** For this route, a Cu salt was dissolved in a solvent (ethanol) in order to get a homogeneous medium, in which C particles were added and dispersed. Then, the solvent was evaporated, giving rise to the homogeneous precipitation of a Cu salt onto the C reinforcements. The final step was related to the calcination in air of the dry material obtained, followed by a reduction step under argon/hydrogen

(Ar/H<sub>2</sub>) at 400 °C (a direct calcination of the dry materials in Ar/H<sub>2</sub> at 400 °C can also be done).

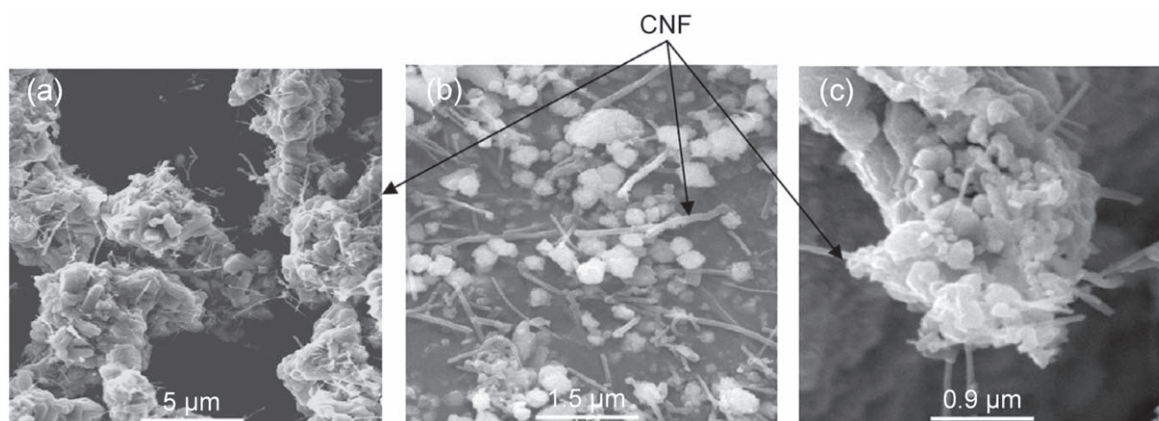
According to the nature of the Cu precursor used, the microstructure of the Cu layer deposited can be quite different, leading to different composite final properties [63].

**3.1.4. Copper chloride (CuCl<sub>2</sub>).** The evaporation of the solvent at 80 °C in air led to the formation of hydrated copper chloride (CuCl<sub>2</sub>, 2H<sub>2</sub>O). The plate-like orthorhombic structure of this precipitated powder can be observed in the SEM micrograph (figure 12(a)). In general, both small size and equiaxed grain shape allowed for uniform coating of fibers. However, the growth of these plate-like structures during this process is not amenable for achieving the desired uniform fiber coating. The calcination of the CuCl<sub>2</sub>, 2H<sub>2</sub>O/C in air at 400 °C gave rise to the formation of cupric oxide (CuO) and then Cu after the reduction step under Ar/H<sub>2</sub> at 400 °C. Grain size of the CuO and/or Cu grain was much smaller than the CuCl<sub>2</sub> plate size. The sublimation process likely occurred during calcinations since Cu particles were observed on the surface of the crucible that was used in the annealing step. Further, the CNF were not uniformly covered, as Cu was present only in spots linked with the fibers. Direct calcinations of CuCl<sub>2</sub>, 2H<sub>2</sub>O in Ar/H<sub>2</sub> at 500 °C (figures 12(b) and (c)) did not change microstructural features, although there was no oxidation step.

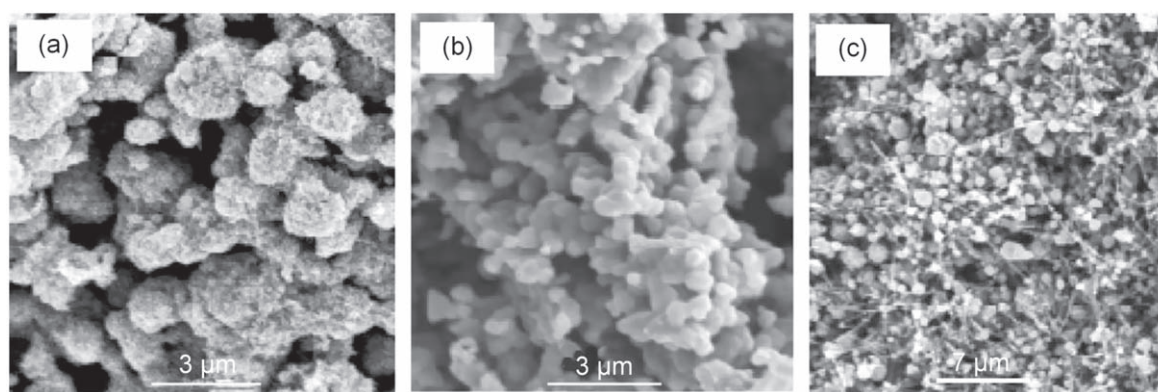
**3.1.5. Copper nitrate (Cu(NO<sub>3</sub>)<sub>2</sub>, 3H<sub>2</sub>O).** After evaporation of the solvent, a hydrated copper nitrate (Cu<sub>2</sub>(OH)<sub>3</sub>(NO<sub>3</sub>)) was deposited onto CNFs with a monoclinic structure. As opposed to the CuCl<sub>2</sub> tetragonal structure, the monoclinic form likely induced no preferential orientation with equiaxed grain shape. The grain size was also in the nanometric range (10–50 nm). With both equiaxed and nanometric grain size, the CNF were fully covered by Cu particles, as illustrated in figure 13(a). Figure 13 shows that, after the heat treatment at 400 °C in air, the Cu<sub>2</sub>(OH)<sub>3</sub>(NO<sub>3</sub>) was completely transformed to the CuO phase. During this heating step, there was no preferential oriented grain growth. Further heat treatment at 400 °C under Ar/H<sub>2</sub> atmosphere led to a reduction of the copper oxide to metallic copper (see figure 13). The average grain size of the Cu particles was around 1 μm. A larger grain size was seen in this step probably because the local temperature due to exothermic decomposition of nitrates was far higher than the average temperature of 400 °C (see figure 13(b)). Most of the CNFs were fully covered by these Cu grains.

Calcination of Cu<sub>2</sub>(OH)<sub>3</sub>(NO<sub>3</sub>) directly at 400 °C under Ar/H<sub>2</sub> led to the formation of metallic copper without CuO in the intermediate stage. The SEM micrograph (see figure 14(c)) shows that the CNFs were not more uniformly covered with Cu. Copper grains in near-spherical shape are found to be attached to the CNFs.

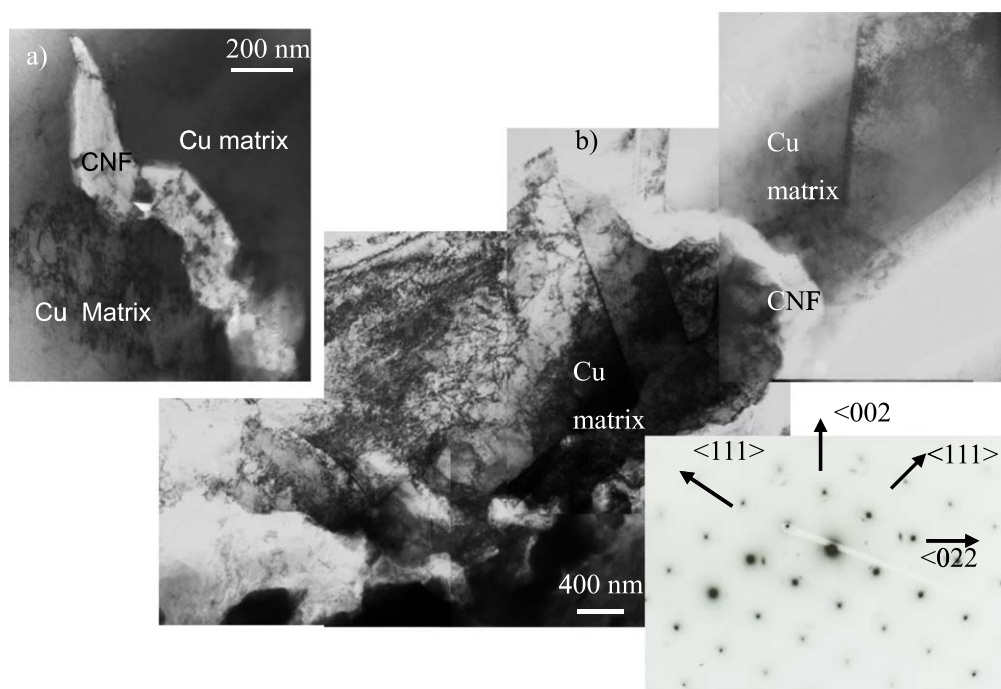
Typical TEM micrographs of densified Cu/CNF materials are shown in figure 14. Several points can be observed: (1) the absence of porosity and/or delamination at the matrix/reinforcement interface and (2) a sharp Cu/CNF interface with a high density of dislocation inside the Cu matrix and



**Figure 12.** SEM micrographs of Cu/CNF microcomposite materials obtained by copper chloride salt decomposition: (a) after solvent evaporation (80 °C, air), (b) after annealing (air at 500 °C + Ar/H<sub>2</sub> at 500 °C), and (c) after annealing (Ar/H<sub>2</sub> at 500 °C). Reprinted from [63], Copyright 2009, with permission from Elsevier.



**Figure 13.** SEM micrographs of Cu/CNF microcomposite materials obtained by copper nitrate salt decomposition: (a) after solvent evaporation (80 °C, air), (b) after annealing (air at 400 °C + Ar/H<sub>2</sub> at 400 °C), and (c) after annealing (Ar/H<sub>2</sub> at 400 °C). Reprinted from [63], Copyright 2009, with permission from Elsevier.

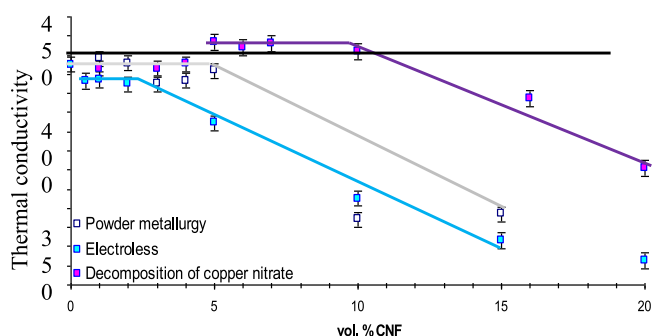


**Figure 14.** TEM micrographs of Cu/CNF(5%) composite materials fabricated using the salt decomposition process. Reprinted from [63], Copyright 2009, with permission from Elsevier.



**Table 5.** Evolution of the surface oxygen content of acid treated CNFs.

Carbon reinforcement	Dispersion in water	Oxygen surface content (XPS)
CNF	No	0.8%
CNF + HNO <sub>3</sub> (12 h)	No	2.2%
CNF + (HNO <sub>3</sub> + H <sub>2</sub> SO <sub>4</sub> 2/3 vol) (2 h)	Yes	11.0%
CNF + (HNO <sub>3</sub> + H <sub>2</sub> SO <sub>4</sub> 2/3 vol) (6 h)	Yes	15.0%

**Figure 15.** Evolution of the thermal conductivity, with the CNF vol.%, of Cu/CNF composite materials. Reprinted from [63], Copyright 2009, with permission from Elsevier.

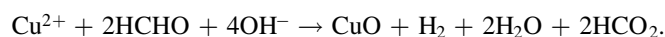
close to the CNFs. Silvain *et al* [62] have shown that dislocations occur due to the thermal stresses induced at the fiber-matrix interface. The different families of dislocations act to reduce the different types of stresses (e.g. shear, normal) and to prevent delamination at the interfaces. In our case, a higher density of dislocations in the Cu matrix was observed, due to the large differential CTE between the CNFs and the Cu. The absence of delamination and presence of dislocations indicated that not only were the thermal stresses large but that the interface was strong due to the presence of chemical bonds built through the surface modified oxygen.

The TC of the Cu/CNF composite prepared through the salt decomposition process is presented in figure 15. It should be noted that the 5 to 10% regime is above the conductivity line for that of Cu. In our opinion, there are three important factors that can affect the conductivity of Cu/CNF composites that are directly affected by the processing method: (1) the distribution of the reinforcement within the matrix, (2) the nature of the interfaces, and (3) the level of porosity. These three requirements were obtained in this case.

**3.1.6. Electroless process.** For this route, the objective was to directly coat the carbon reinforcements with Cu using the conventional electroless process. Localized catalytic centers had to be created on the CNFs surface, as they helped to initiate electroless metal deposition. Palladium (Pd) clusters chemisorbed on the substrate surface constituted these sites.

In a first step, the CNFs were chemically treated using different acid baths in order to create oxygenated sites on the CNFs' surface and to have a good dispersion of the CNFs in water. The conventional electroless process followed in a second step with: (1) a sensitization stage (Sn absorption), (2) an activation stage (Pd absorption), and (3) the plating

stage (Cu deposition) [64–66]. It consisted of the successive immersion of the CNFs into the corresponding baths by diluting solutions of tin(II) chloride (SnCl<sub>2</sub>) (sensitization), palladium(II) chloride (PdCl<sub>2</sub>) (activation), and an aqueous mixture of copper sulfate (CuSO<sub>4</sub>), potassium sodium tartrate tetrahydrate (KNaC<sub>4</sub>H<sub>4</sub>O<sub>6</sub>·4H<sub>2</sub>O), sodium hydroxide (NaOH), and HCHO (plating). HCHO initiates the coating deposition by reducing the CuSO<sub>4</sub> according to the following reaction:



The main parameters involved in this process are: (1) the pH of the solution ranging from 9 to 12, (2) the deposition time, (3) the temperature of the different baths, and (4) the reaction rates.

The acid pretreatment is of first importance to ensure a good electroless deposition through the presence of oxygen sites. As an example, the effects of two different acid treatments were investigated using XPS to determine the evolution of the oxygen (O) and C species onto CNFs [67]. Table 5 clearly shows that mixed nitric and sulfuric acids (HNO<sub>3</sub> + H<sub>2</sub>SO<sub>4</sub>) have to be used in order to increase oxygen content and allow a good dispersion in water.

The coating conditions can induce large changes in the microstructural features of the coated CNFs. Figure 16 shows the CNF evolution as a function of pH (CNFs were treated with an acid solution (HNO<sub>3</sub> (1/3 vol) + H<sub>2</sub>SO<sub>4</sub> (2/3 vol)) for 6 h before electroless coating). The pH of the solution was actually one of the key factors in obtaining a homogeneous Cu coating around each CNF. For a pH lower than 12, no coating was observed (figure 16(b)), while a homogeneous coating was obtained for a pH greater or equal to 12 (figure 16(c)). The coating thickness was controlled by manipulating parameters, such as CuSO<sub>4</sub> concentration, deposition time, and CNF content. The Cu coating was more homogeneous when: (1) the reducer concentration (HCHO) was increased and (2) the water content of the solution was increased. Both conditions led to a decrease in the coating rate. Whatever the conditions, an increase of the bath temperature was always observed; and the pH of the solution decreased during the deposition bath. The exothermicity of the reaction was linked with the CNF concentration within the bath.

Typical TEM micrographs of fully dense Cu/CNF materials prepared by the electroless process and uniaxially hot pressed, are shown in figure 17. The black and gray lines are all associated with CNFs (figure 17(a)). Relatively good dispersion of the CNFs inside the Cu matrix can be seen,

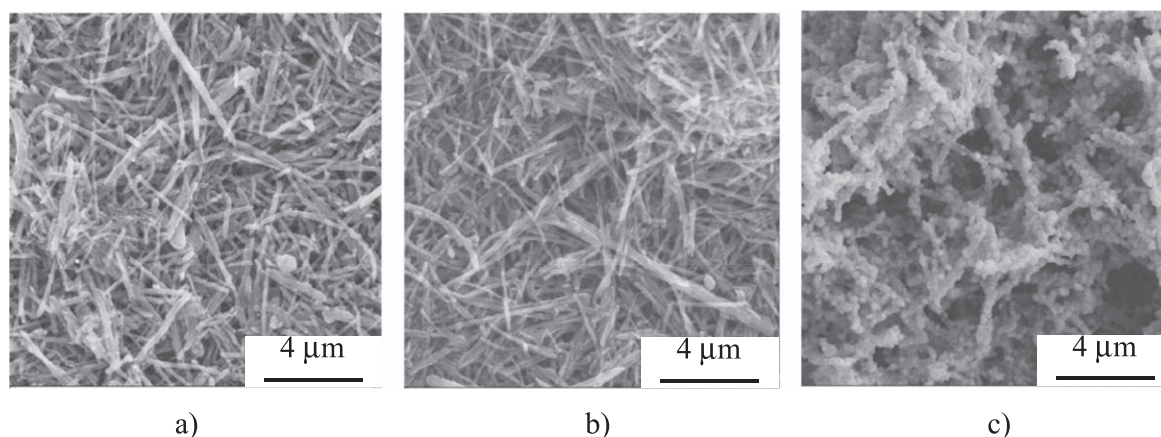


**Figure 16.** Evolution of the coating behavior with the pH of the solution (coating time 30 min): (a) noncoated CNF, (b) pH = 10, and (c) pH = 12. Reproduced with permission from [67]. © (2007) Trans Tech Publications, Switzerland.

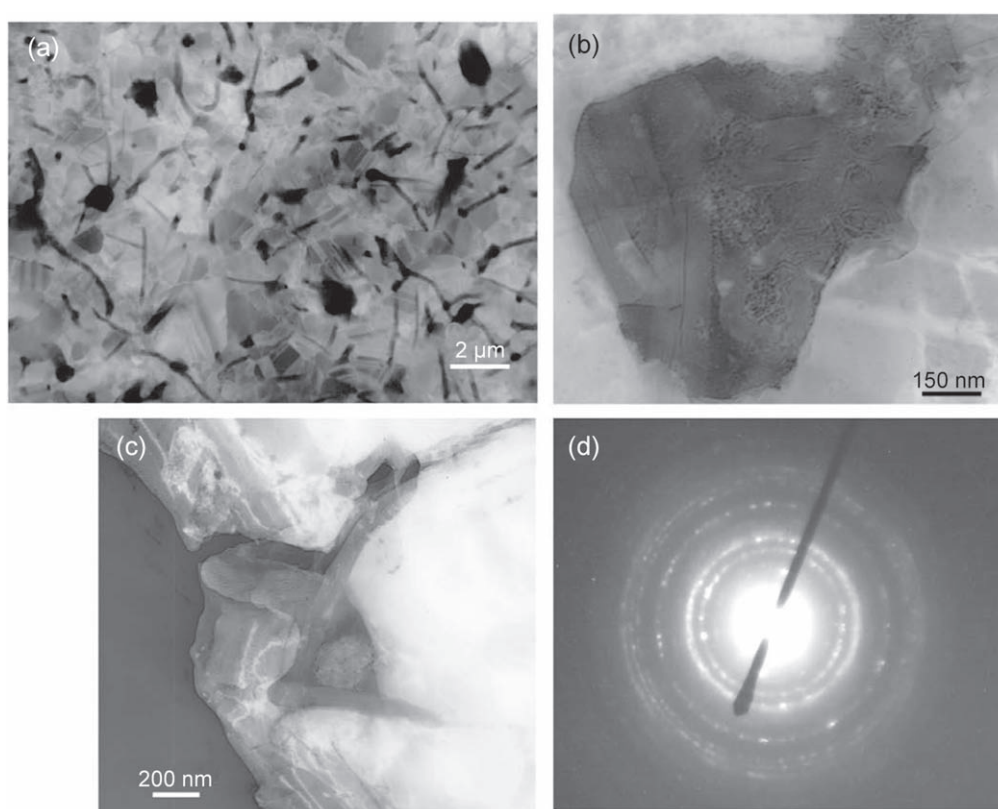


**Figure 17.** TEM micrographs of Cu/CNF(5%) composite materials fabricated using an electroless process and uniaxial hot pressing. Reprinted from [63], Copyright 2009, with permission from Elsevier.

although some agglomerated CNFs (black spots) can still be observed (figures 17(a) and (b)). The cavities seen in figure 17(c) correspond to locations left by CNFs. The diffraction pattern seen in figure 17(d) clearly shows that the Cu grain size was nanometric in scale and was the result of the electroless deposition process. Similar to that for the conventional powder-metallurgy-processed materials, there was no grain growth in Cu induced by this densification step.

The TC of the Cu/CNF composite prepared through the electroless process is presented in figure 15. The lowest TC

values measured were attributed to the high density of Cu grain boundaries linked with the nanosized of the Cu grains.

**3.1.7. Deposition of Cu nanoplots onto C.** Another technique for making a Cu matrix compatible with C is the deposition of Cu nanoplots onto C reinforcements. This process first involved a surface treatment with a phosphoric agent, then an annealing treatment in air, and finally a reducing heat treatment under controlled atmosphere (Ar/H<sub>2</sub> 5 vol.%). The

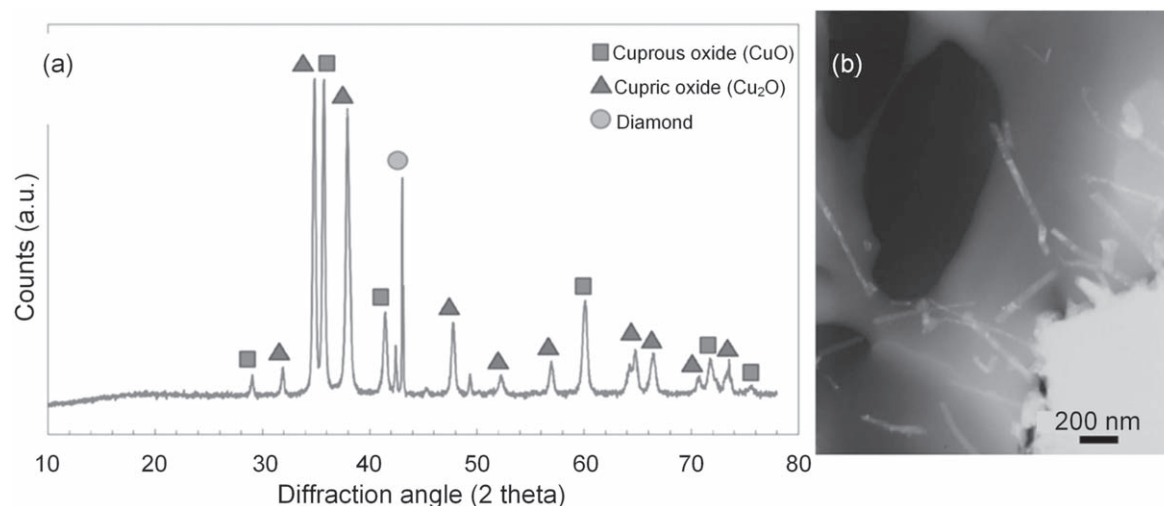


**Figure 18.** (a) X-ray diffraction diagram of D covered with Cu oxidized by the first annealing step and (b) TEM micrograph of CuO nanowires on D. Reprinted from [68], Copyright 2012, with permission from Elsevier.

deposition of Cu nanoparticles occurred during the last step [68].

The surface treatment was based on the functionalization of the C reinforcement by a phosphoric reagent. This surface treatment has been applied on different sort of carbon, i.e. carbon fiber, graphite flakes and diamond particles. It can be processed in the following ways, based on the nature and the chemical reactivity of the reinforcement. One process consists of immersing the reinforcement in a solution of orthophosphoric acid (H<sub>3</sub>PO<sub>4</sub>) for 30 min at 80 °C. The second process consists of mixing an ester phosphate with the CFs or particles, Cu powder, and a solvent in a 3D mixer for 4 h. For example, CFs are not well functionalized by ester phosphate, whereas phosphoric acid allows a modification of the CNF surface and the fixation of P species.

After chemical treatment, carbon reinforcements mixed with Cu powder were annealed under air at 400 °C for two hours. After this oxidation step, the surface of the C was still functionalized, but no nanoparticles were detected on it. However, the oxidized Cu particles exhibited a very peculiar nanowire-shaped morphology (figure 18(b)). Such a phenomenon was already observed by Jiang *et al* [69]. X-ray diffraction analysis of the oxidized powder (figure 18(a)), combined with a TEM diffraction pattern of one of these nanowires showed that these nanostructures were made of CuO. A step-by-step kinetic study of the growth process showed that the CuO nanowires started appearing when the temperature reached 400 °C and grew continuously as the annealing time increased, reaching lengths of several microns after two hours of annealing. It is assumed that the formation of these CuO nanowires was driven by the thermal oxidation of Cu during annealing.

Nucleation and growth of copper particles on the substrate surface was processed during the second annealing step under reducing atmosphere (Ar/H<sub>2</sub> 5 vol.%). This phenomenon only occurred at locations of the substrate where phosphoric treatment was performed. The H<sub>3</sub>PO<sub>4</sub> solution was dropped along a line on a Si wafer (leading to the

presence of phosphorus atoms bonded to the surface). After the reduction step, the wafer was covered by Cu particles strictly along the line where the functionalization occurred.

Figure 19 shows typical micrographs of functionalized CFs after reduction at 400 °C for different annealing times: 10 min (figure 19(a)), 30 min (figure 19(b)) and 1 h (figure 19(c)). Table 1 gives the average size of the Cu particles deposited onto these CFs as a function of annealing time. It can be observed that short annealing times (less than 40 min) lead to elongated Cu particles, with an aspect ratio close to two. The particles tend to become spherical when annealing gets longer which suggests that the growth occurs from the vapor phase in conditions near the thermodynamic equilibrium, since a hemispherical shape helps to reduce an excess of surface energy. This is supported by the observations at higher magnification of Cu particles after the longest annealing time. The particles were not exactly spherical but polyhedrons with several facets. This kind of morphology matches the equilibrium shapes described by Wulff where surfaces presenting the lowest free surface energy are favored during the growth of crystalline particles. A simple Ostwald ripening mechanism, through vapor phase diffusion, could explain the growth and the shape of the Cu particles deposited on the chemically treated substrates. Under reducing atmosphere, the CuO nanowires sublime first, due to their very low curvature radius. When the vapor pressure reaches the saturation vapor pressure of Cu, it condenses preferentially on the reactive sites of the functionalized substrate. The largest particles then grow at the expense of the smallest, and their shape evolves towards the equilibrium according to the surface tensions of the system.

The size of the Cu particles ranged from 10 nm to 1 micron and can be adjusted as a function of experimental parameters and the nature of the substrate. Actually, the size of Cu particles is related to the number of nuclei initially present per surface unit. When this number is high, the final size of the Cu particles can reach one micron because of particle coalescence, along with vapor growth. On the



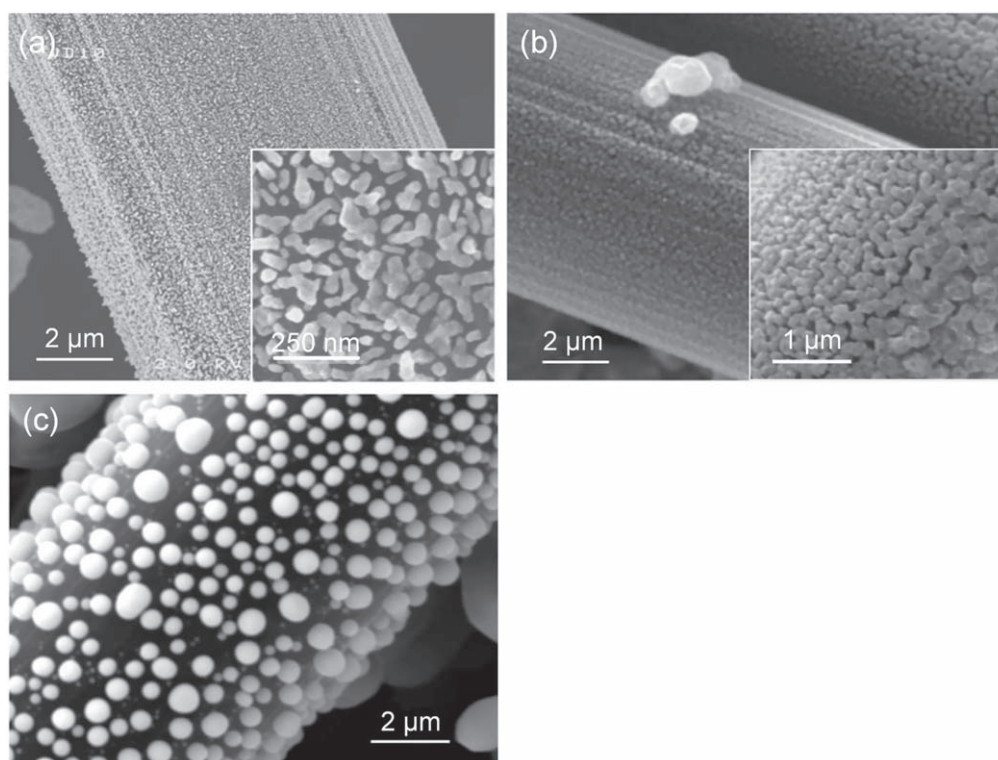


**Figure 19.** Growth of Cu particles onto CF substrate for different annealing times: (a) 10 min; (b) 30 min, and (c) 60 min. Reprinted from [68], Copyright 2012, with permission from Elsevier.

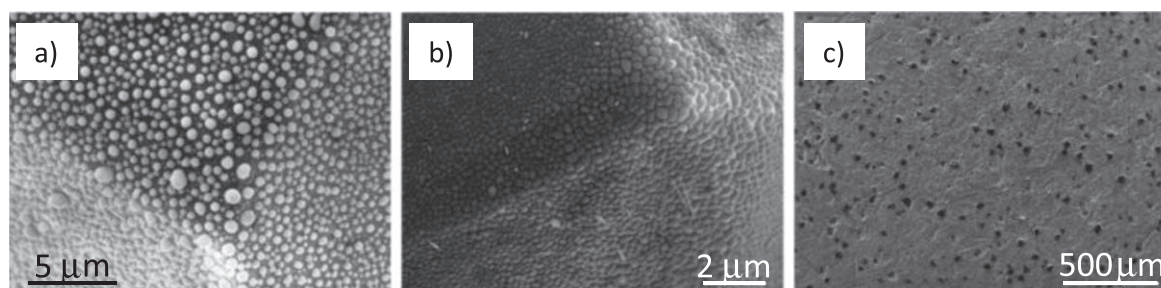


**Figure 20.** (a), (b) SEM micrographs of Cu dots on D particles. (c) SEM micrograph of Cu/D (Cu) composite materials. [70] John Wiley & Sons. © 2017 WILEY-VCH Verlag GmbH & Co. KGaA, Weinheim.

contrary, for the same flux of matter in the vapor phase but with a lower number of nuclei, the particles are too far from each other to coalesce during annealing; and the final particle sizes remain in the nanometric range. This was the case of a medium grade CF functionalized by orthophosphoric acid. When a diluted solution of water- $\text{H}_3\text{PO}_4$  (1:1) was used at a temperature of  $80^\circ\text{C}$  for 30 min, the phosphorus was hardly detected by XPS. The resulting Cu particles deposited on the CF after deoxidization were smaller than 300 nm in diameter. Conversely, when the same functionalization treatment was done on high grade CFs, which are more sensitive to acid attack, XPS analysis revealed the presence of 10 at.% of phosphorus at the surface of the fiber; and the Cu particles were larger. These results highlight the strong correlation between the amount of phosphorus bonded to the substrate and the size of the deposited Cu particles. The conclusion was the same when the ester phosphate was used as functionalizing agent. The amount of ester phosphate reacting with the

substrate can be adjusted by changing the functionalization time. For example, a mixing time of 4 h leads to particles that do not exceed 500 nm in size. When the fibers are in contact with the functionalizing agent for 24 h, Cu particles can reach  $2\ \mu\text{m}$ .

High densities were obtained when a pure Cu/D composite powder mixture and a Cu/D(Cu) composite powder mixture were densified at  $650^\circ\text{C}$  under vacuum (figure 20). The materials were maintained under HP for 30 min.

Consistent with their low compaction level, pure Cu/D composites exhibited low TC (figure 21(a):  $\lambda_{\text{Pure Cu/D}} = 260\ \text{W m}^{-1}\ \text{K}^{-1}$ ). The relatively high porosity level of these composites (6.6%) led to heat transfer loss and critically degraded their thermal conduction performance. The Cu-B/D composites (figure 21(b):  $\lambda_{\text{Cu-B/D}} = 440\ \text{W m}^{-1}\ \text{K}^{-1}$ ) and Cu-Cr/D composites (figure 21(c):  $\lambda_{\text{Cu-Cr/D}} = 500\ \text{W m}^{-1}\ \text{K}^{-1}$ ) exhibited strongly enhanced TCs relative to pure Cu/D

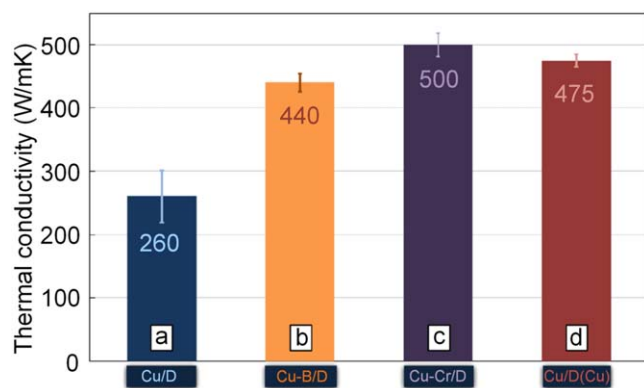


**Figure 21.** Influence of interfacial bonding on the thermal conductivity of the Cu/D materials. Reproduced with permission from [56].

composites processed without any bonding solution. In the same manner, average TC results obtained from Cu/D(Cu) composites fabricated through the innovative Cu coating process (figure 21(d):  $\lambda_{\text{Cu/D(Cu)}} = 475 \text{ W m}^{-1} \text{ K}^{-1}$ ) demonstrated that Cu particles deposited onto D reinforcements prior to sintering effectively acted as chemical bonding agents between D and the Cu matrix and enabled efficient interfacial heat transfer between electronic and phononic heat conduction. The Cu/D(Cu) composites exhibited TC superior to that of Cu-B/D composites and comparable to that of Cu-Cr/D composites. These results demonstrate the primary role played by interfacial chemical bonding, either through carbide interphases or Cu coating of D, on the heat transfer process at the Cu/D interface in Cu/D composite materials. Indeed, the use of  $\text{B}_4\text{C}$ , Cu coating, and  $\text{Cr}_3\text{C}_2$  bonding solutions at the Cu/D interface led to an increase in TC of 70%, 82%, and 92%, respectively, relative to the TC of pure Cu/D composites.

The process exhibits high reproducibility and the final material consists in a substrate fully covered with nanometric to submicronic Cu particles whose density, size, and shape depend on experimental conditions.

### 3.2. Base-plate composites fabricated using liquid phase sintering

Contrary to solid state powder metallurgy processes, liquid phase sintering allows both solid and liquid phases to coexist during the fabrication process. For the composite materials fabricated in this work, the liquid phase consisted of a Cu-titanium (Ti) alloyed powders while the solid phase consisted of Cu dendritic powders and CF reinforcements. The Cu-Ti alloy should present a melting point lower than that of pure Cu. Therefore, the composition of the Cu-Ti alloyed powders corresponded to the composition of the eutectic transformation which occurred at  $884^\circ\text{C}$  for a Cu composition of 73.5 at%. The sintering temperature was set to  $950^\circ\text{C}$ , lower than the melting point of Cu ( $1083^\circ\text{C}$ ). One interesting point of this process is that the liquid can flow around the grains and infiltrate the pores created by the intertwining of CFs (a downside of regular net-shaped processes with high reinforcement content). Furthermore, the diffusion and reactivity of

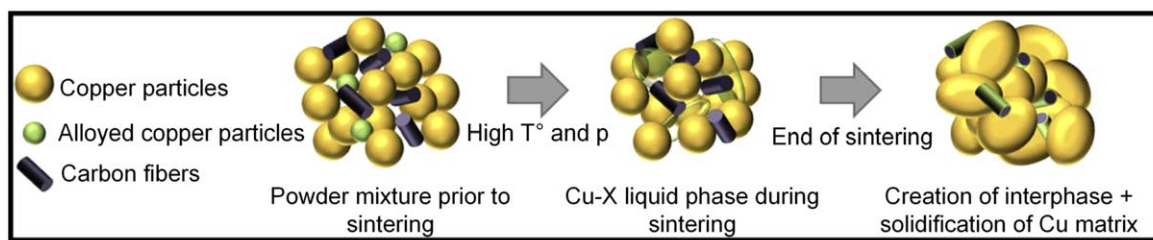
the carbide-forming species was enhanced, which allowed the carbide to be formed at lower temperatures and shorter time periods. A schematic of the solid-liquid co-existent phase process is shown in figure 22. The  $\text{Cu}(\text{Cu-Ti})_x/\text{CF}$  composites prepared using liquid phase sintering were compared to Cu/CF composites fabricated without Cu-Ti powders. The amount of liquid Cu-Ti phase varied from 2 to 10 vol.%.

Figure 23 shows the SEM micrographs of liquid phase sintered Cu/CF composites. The chemical contrast offered by the BSE mode of the SEM allows the interfacial zone surrounding the CFs to be distinguished. The interphase created appears to be homogeneous and was present on a large amount of CFs. An EDS line scan across a coated CF, shown in figure 24, shows that the interfacial zone between the Cu matrix and the CF was rich in Ti. In addition, little or no Ti signal was observed in the matrix region which suggests that most of the Ti diffused to the CFs. To confirm this hypothesis, high-resolution XRD data were collected for a 2-theta range between  $30$  and  $65^\circ$  on a bulk  $\text{Cu/TiC}_x/\text{CF20}$  composite. Le Bail type structural refinement was carried out to determine the lattice parameters of the Cu matrix. The XRD pattern is shown in figure 25. There was no significant difference between the theoretical and the experimental lattice parameters which, therefore, confirmed the absence of a solid solution of Ti in Cu for this composite.

Theoretical TC values of Cu/CF composite materials were calculated using the Fricke model [72]. The TCs obtained using the Fricke model, for the composites without Cu-Ti and with 4 vol.% of Cu-Ti, are shown in figure 26. As expected, the TC decreased as the CF content increased since the CF conductivity was lower than that of the Cu matrix. The first observation is the drastic decrease in TC for 10 vol.% CF when 4 vol.% Cu-Ti was present in the material. The poor TC can be explained by the fact that there was not enough C within the composite to allow complete diffusion of the Ti towards the C. Therefore, Ti had a tendency to remain in the Cu matrix as a solid solution. This tendency was verified by structural refinement of a high quality XRD pattern of the  $\text{Cu/TiC}_x/\text{CF10}$  composite. Only Cu peaks were observed, and the calculated lattice parameter was equal to  $3.62427(5)$  (Bragg R-factor of 0.184). We concluded that the expansion of the lattice was caused by the presence of Ti in a solid solution and explained the poor TC observed for 10 vol.% of CF. It is known that the transport properties (thermal and electrical conductivities) of Cu-Ti solid solutions are lower than those of pure Cu. For example, for a solid solution of Ti in Cu that reaches 0.04 wt%, the electrical conductivity is much lower than that of pure Cu [73]. For CF content that exceeded 20 vol.%, the TCs of composites containing 4 vol.% of Cu-Ti were higher than those without Cu-Ti. However, the values obtained for both composite materials were always lower than the TC values calculated with Fricke's model.

One can also observe the important slope mismatch between the Fricke model points and the measured points obtained for composites sintered with and without Cu-Ti. This mismatch is indicative of the poor accuracy of the Fricke model for our composites. Indeed, the slope deviation here indicates that the CF orientation and the average assumed TC





**Figure 22.** Schematic of the liquid phase sintering process. The initial powder mixture (Cu + Cu-Ti + CF) was sintered under 40 MPa at 950 °C. During the sintering plateau of 30 min, the Cu-Ti liquid phase was generated. At the end of the sintering program, the CFs were coated with a TiC interphase and were oriented in the plane perpendicular to the pressure axis. Reprinted from [71], Copyright 2018, with permission from Elsevier.

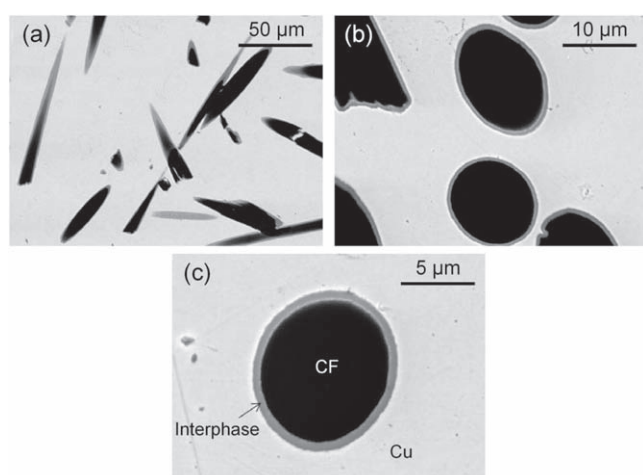


**Figure 23.** SEM micrographs in BSE mode of Cu/TiCx/CF composites sintered with (a) 4, (b) 8, and (c) 10 vol.% of Cu-Ti alloyed powders. Reprinted from [71], Copyright 2018, with permission from Elsevier.

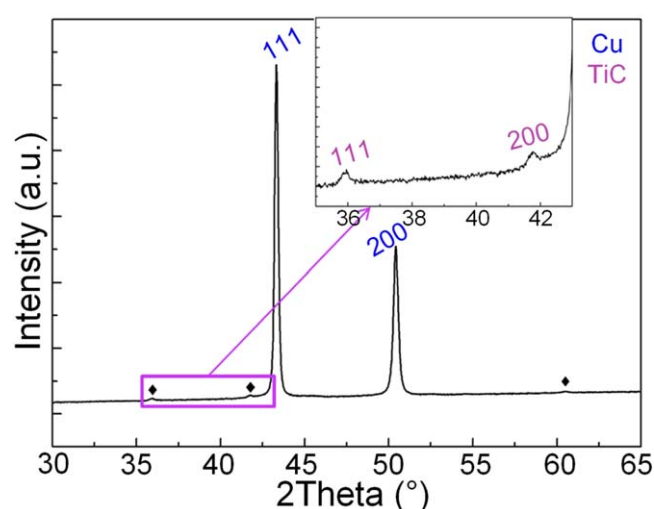


**Figure 25.** XRD pattern obtained from a Cu/TiCx/CF (20 vol.%) composite pellet. Reprinted from [71], Copyright 2018, with permission from Elsevier.

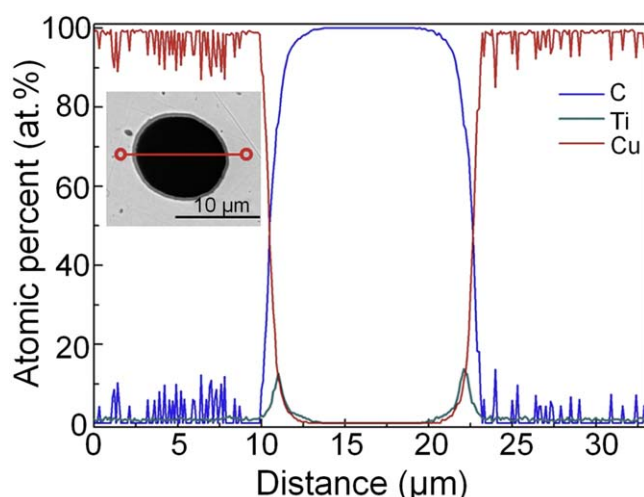


**Figure 24.** EDS line scan obtained through the cross-section of a CF coated with a Ti-based interphase inside the Cu matrix. Reprinted from [71], Copyright 2018, with permission from Elsevier.

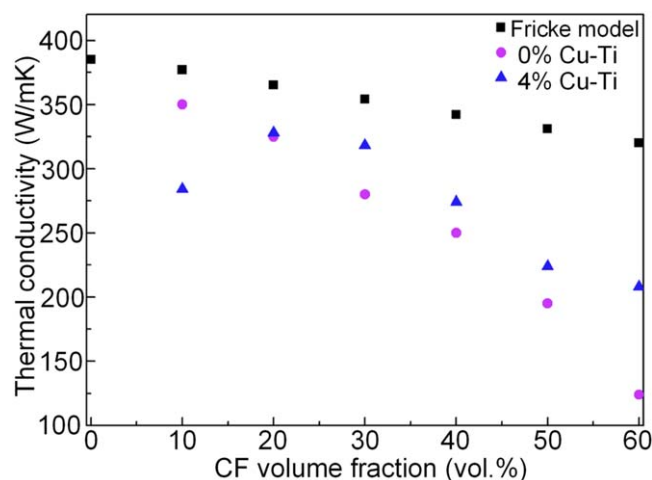


**Figure 26.** Thermal conductivity values obtained for composites with and without 4 vol.% of Cu-Ti, as well as theoretical values obtained with the Fricke model. Reprinted from [71], Copyright 2018, with permission from Elsevier.

of  $277.5 \text{ W m}^{-1} \text{ K}^{-1}$  are not realistic. The deviation between the two types of composites can be explained by the creation of a strong interfacial bonding between the CF reinforcements and the titanium carbide (TiC) interphase (covalent bonding),

as well as the one between the TiC interphase and the Cu matrix (metallic). The creation of such chemical interphases, in comparison with the mechanical one induced during cooling by the difference in CTEs between the CF and the Cu

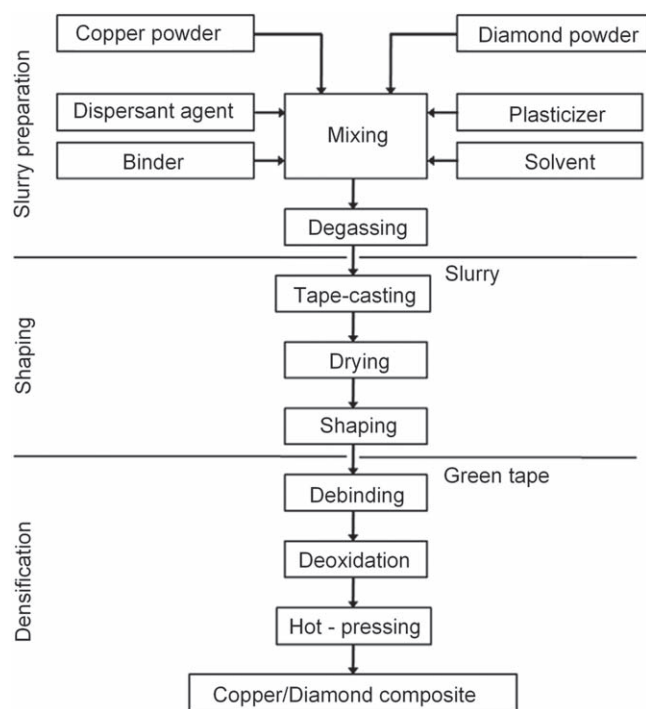


**Figure 27.** Processing flowchart of the D-reinforced Cu matrix composite films. Reprinted from [76], Copyright 2012, with permission from Elsevier.

matrix in the liquid-phase-sintered materials, improves the heat transfer from the matrix to the reinforcement and vice versa thereby increasing the final TC of the composite materials.

### 3.3. Base plate composite fabricated by tape casting

The tape casting process offers an original solution for fabricating thin sheets of composites. The tape casting process is currently industrially employed to produce thin or multi-layered ceramic structures for numerous applications (aluminum oxide ( $\text{Al}_2\text{O}_3$ ) and aluminum nitride ( $\text{AlN}$ ) for electronic devices, barium titanite ( $\text{BaTiO}_3$ ) for capacitors, solid electrolytes for sensors or energy conversion, and piezoelectric ceramics for actuators and transducers). It features many advantages: (1) low cost, (2) accurate thickness control, (3) smooth surface finish, (4) material net shaping, and (5) large-scale capability [74]. In addition, it also enables a uniform dispersion of D particles into the Cu matrix, which prevents eventual segregations due to the difference of density between Cu and D powders during the mixing step [75].

**3.3.1. Processing of the composite materials.** The tape casting process (figure 27) consists of preparing a suspension of inorganic powders in an aqueous or nonaqueous system. This slurry is a complex, multicomponent system typically containing powder (metallic and/or ceramic), solvent, binder, dispersant agent, and plasticizer. The suspension must be stable, homogeneous, and with a suitable rheological behavior according to the tape-casting process. The slurry is spread onto a support by means of a motorized doctor blade. After

evaporation of the solvent, the dried tape obtained, or green tape, is cut to the desired shape. The composite tape is then heat treated, densified, and characterized.

**3.3.2. Microstructure of composite tapes.** Figure 28(a) shows a SEM micrograph of a Cu/D green tape before sintering. The organics remaining after solvent evaporation (i.e. binder, plasticizer, and dispersant) are removed during a debinding step of 2 h at 400 °C under air. The air atmosphere enables efficient elimination of organics but oxidizes the Cu matrix, which leads to the formation of nanosized, wire-shaped CuO structures on the dendrites, as shown in figures 28(b) and (c). The reducing treatment under  $\text{Ar}/\text{H}_2$  leads to the sublimation of the CuO nanowires, which are formed on the surface of the dendritic copper powder during the oxidation of the copper matrix, through a solid-vapor process [77]. The most important post-treatment feature is that the diamond powders are coated by copper particles with submicronic sizes as shown in figures 28(d)–(g). The coverage of the D surface by the Cu particles is remarkably uniform. Moreover, the size of the Cu particles deposited on the D surface can be adjusted by tuning the reduction time and temperature, as shown in figures 28(d) and (e) with Cu particle sizes ranging from 400 nm to 1  $\mu\text{m}$  (after 60 min at 400 °C under  $\text{Ar}/\text{H}_2$ ); and in figure 28(f) with Cu particle sizes ranging from 300 to 800 nm (after 5 min at 400 °C under  $\text{Ar}/\text{H}_2$ ); and figure 28(g) with Cu particle sizes ranging from 100 nm to 400 nm (after 1 min at 350 °C under  $\text{Ar}/\text{H}_2$ ) figures 28(h) and (i).

**3.3.3. Thermal conductivity.** As shown in figure 29, the average TC of composites increased regularly from 364 to 455  $\text{W m}^{-1} \text{K}^{-1}$  with respect to D volume fractions ranging from 0% to 40%, which confirms that the Cu particles deposited onto the D reinforcements prior to sintering effectively acted as chemical bonding agents between the D and the Cu matrix. It enabled efficient interfacial heat transfer between electronic and phonon conduction. However, a drop in TC was observed to 320  $\text{W m}^{-1} \text{K}^{-1}$  with a D volume fraction of 50% due to the low final density of the  $\text{Cu}_{50}\text{D}_{50}$  composite, which is critically detrimental to the TC. This decrease in TC means that the percolation threshold (i.e. the reinforcement volume fraction at which exists a continuous path between reinforcements into the composite) had been reached. The percolation threshold was located between 40% and 50% in the D volume fraction.

Experimental values can be compared to theoretical values predicted by Maxwell's model [78]. This model predicts the TC of composites, assuming that the reinforcements are strictly spherical, that the reinforcement volume fraction is low (dilute medium), and that no thermal boundary resistance exists at the Cu/D interface. However, the significance of the theoretical values predicted by Maxwell's model is affected by the fact that the precise TC of the D powders is unknown; it was assumed to be equal to 1000  $\text{W m}^{-1} \text{K}^{-1}$ . Despite this uncertainty, the evolution of experimental TCs follows that of the theoretical TCs predicted by Maxwell's model. However, the gap between



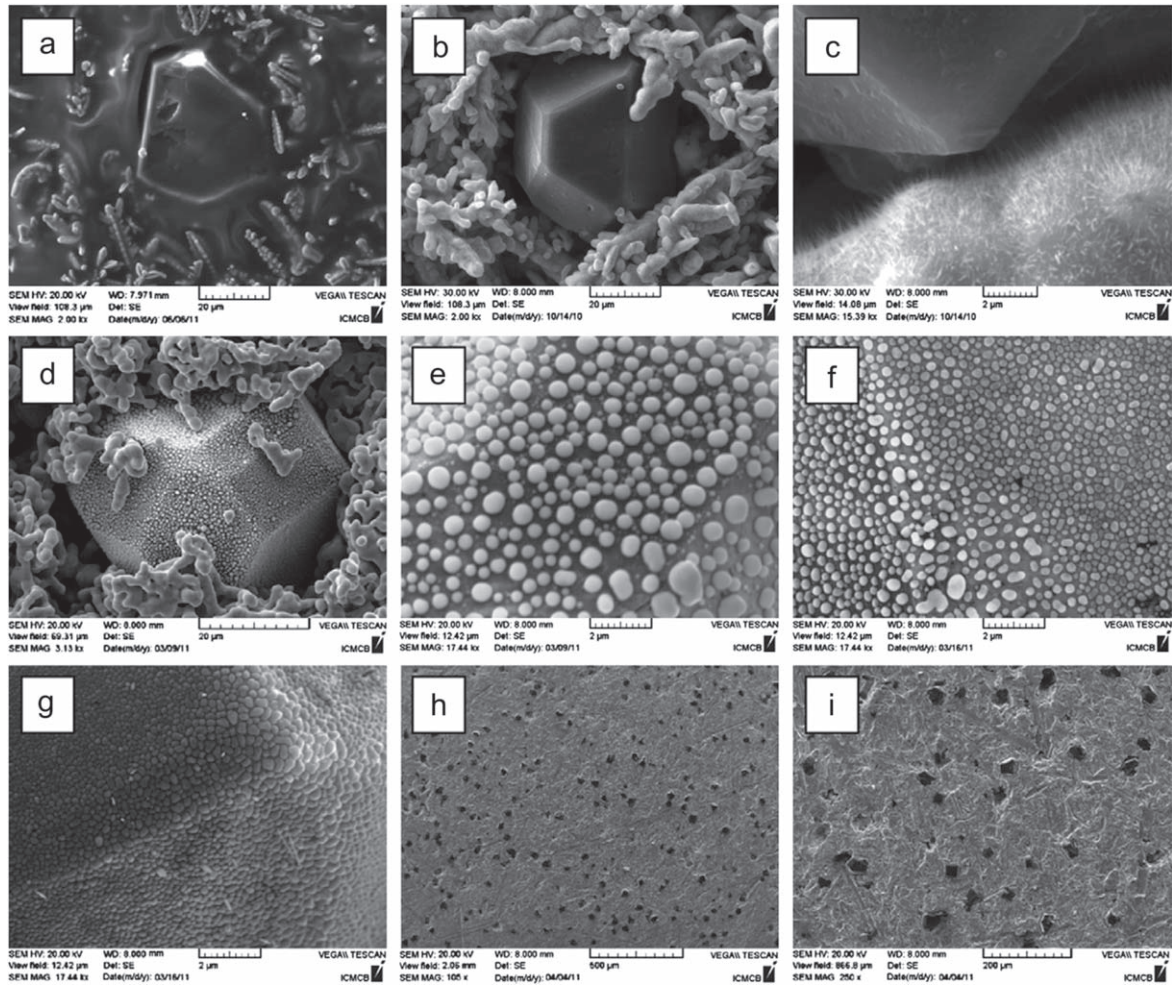


**Figure 28.** Step-by step SEM micrographs of the Cu/D composite tape: (a) after tape casting, (b) and (c) after debinding, (d) and (e) after deoxidation during 60 min at 400 °C, (f) after deoxidation during 1 min at 400 °C, (g) after deoxidation during 1 min at 350 °C, and (h) and (i) after hot pressing (20 vol.% D). Reprinted from [76], Copyright 2012, with permission from Elsevier.

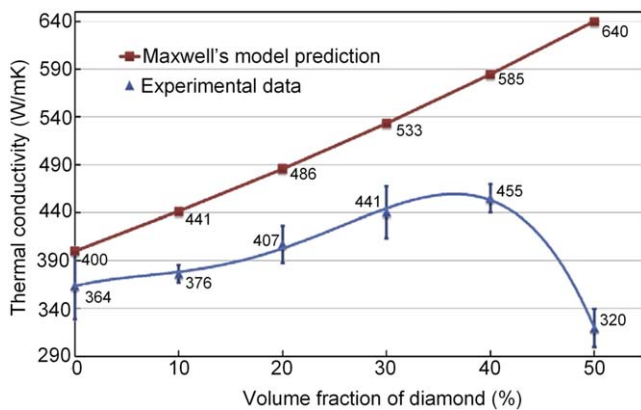


**Figure 29.** Modeled and experimental thermal conductivity of the D-reinforced Cu matrix composite films as a function of D volume fraction. Reprinted from [76], Copyright 2012, with permission from Elsevier.

the measured TCs and those calculated remains important. It can be related to two points: one is the interfacial thermal resistances of layer interfaces in stack; another is the interfacial thermal resistance between D and Cu. The TC

measured with a pure Cu sample made by this tape casting process is only  $363 \text{ W m}^{-1} \text{ K}^{-1}$  instead of the theoretical value of  $400 \text{ W m}^{-1} \text{ K}^{-1}$ . This decrease can be attributed to the interfacial thermal resistances of layer interfaces in stack. Although no distinction can be made between the layers through electronic micrograph, the TC of the stack decreased when the number of tapes by stack increased. The interfacial thermal resistance between D particles and the Cu matrix may also contribute to a decrease the TC. The existence of porosity or voids at the matrix/reinforcement interface would degrade the thermal properties of the composites. In addition, the nonspherical shape of D particles is likely favorable to increase the gap between experimental and Maxwell's model values. Finally, we observe that the deviation from Maxwell's prediction increases with D volume fraction since the validity of the dilute medium assumption is affected with increasing D volume fraction. Nevertheless, we reached an average TC of  $455 \text{ W m}^{-1} \text{ K}^{-1}$  and a maximum TC of  $480 \text{ W m}^{-1} \text{ K}^{-1}$  with a D volume fraction of 40%, which is a significant improvement relative to pure Cu ( $k_{\text{Cu}} = 400 \text{ W m}^{-1} \text{ K}^{-1}$ ).

## 4. Conclusion

The electronic industry is involved in an endless search for new materials that enable electronic systems with increasing density of components, through higher heat dissipation capability, lower density, and higher reliability while matching the CTE of materials currently used in electronic packaging components, ceramic substrates, Si, silicon carbide (SiC), and other semiconductors, etc. In fact, reliability now appears to be one of the major problems affecting the electronics, microelectronics, telecom, automotive, and aeronautic industries.

Thermal management is an increasingly critical part of achieving competitive functionality in these industries since it impacts the speed, size, weight, and reliability of components, especially for future components which will need to dissipate heat from electric currents and packaging densities an order of magnitude higher than those in use today. Due to the high power dissipation capability of current and future electronic semiconductors and the high demand for high reliability, new conductive composite materials with adapted TC and CTE must be developed in order to: (1) control and lower the temperature of the electronic component and (2) adjust the thermal stresses between the different layers of typical electronic devices. The Cu/C composites are such attractive materials for thermal conduction because of their high TC and low CTE. Their potential primary applications are heat sinks, thermal planes, and substrates.

The properties of Cu/C composites depend mainly on conditions and route processes. Today, the powder metallurgy processes offer Cu/C composites with a low cost of elaboration, a low CTE, and excellent TC properties. However, physical properties obtained by the powder metallurgy process, such as CTE and TC, are strongly anisotropic. In addition, the lack of interfacial strength between Cu and C requires either a previous surface treatment of the C species and/or the addition of an alloying carbide element inside the Cu matrix in order to improve the interface properties between Cu matrix and C species. Different examples of Cu/C composite materials with different C type (CF, CNF, D) and different C coatings and processing routes have been shown. The positive effect of the C surface treatment and the addition of carbide-forming species inside the Cu matrix on the TC and the CTE of the composite materials have been demonstrated. It has also been clearly shown that the presence of chemical reaction zone, at the Cu–C interface, has a positive effect on TC evolution with the number of thermal cycles whereas for pure mechanical bonding MMCs, induce by the CTE difference between the matrix and the reinforcement, degradation of the thermal properties have been measured. The chemical and microstructural properties of the interfacial zones have been correlated with the fabrication process and the final macroscopic properties of the composite materials.

## ORCID iDs

Jean-François Silvain  <https://orcid.org/0000-0002-5881-6833>

## References

- [1] Luedtke A 2004 *Adv. Eng. Mater.* **6** 142
- [2] Zweben C 1998 *JOM* **50** 47
- [3] Geffroy P-M and Silvain J-F 2007 *Mater. Sci. Forum* **534** 1505
- [4] Mathias J-D, Geffroy P-M and Silvain J-F 2009 *Appl. Therm. Eng.* **29** 2391
- [5] Korb G, Buchgrader W and Schubert T 1998 IEEE/CPMT Berlin Int. Electronics Manufacturing Technology Symp. (27–28 April 1998)
- [6] Zweben C 2006 *Adv. Packag.* **15** 20
- [7] Vincent C 2008 *PhD Thesis* University of Bordeaux, France
- [8] Veillère A 2009 *PhD Thesis* University of Bordeaux, France
- [9] Silvain J-F, Denis-Lutard V, Geoffroy P-M and Heintz J-M 2010 *Mater. Sci. Forum* **631–2** 149
- [10] Sun S J and Zhang M D 1991 *J. Mater. Sci.* **26** 5762
- [11] Koráb J, Štefánik P, Kavecký Š, Šebo P and Korb G 2002 *Composites A* **33** 577
- [12] Buchgrader W, Korb G, Schubert T and Kempf B 2006 *Microstructural Investigation and Analysis* (Weinheim: Wiley) pp 150–5
- [13] Silvain J-F, Veillère A and Lu Y 2014 *J. Phys.: Conf. Ser.* **525** 012015
- [14] Yoshida K and Morigami H 2004 *Microelectron. Reliab.* **44** 303
- [15] Yuan S Q, Shen F, Chua C K and Zhou K 2018 *Prog. Polym. Sci.* **91** 141
- [16] Xia L, Jia B, Zeng J and Xu J 2009 *Mater. Charact.* **60** 363
- [17] Kang Q, He X, Ren S, Zhang L, Wu M, Guo C, Cui W and Qu X 2013 *Appl. Therm. Eng.* **60** 423
- [18] Rambo C R, Travitzky N and Greil P 2015 *J. Compos. Mater.* **49** 1971
- [19] Qu X, Zhang L, Wu M and Ren S 2011 *Prog. Nat. Sci.-Mater.* **21** 189
- [20] Chu K, Jia C, Guo H and Li W 2013 *J. Compos. Mater.* **47** 2945
- [21] Schubert T, Trindade B, Weißgärber T and Kieback B 2008 *Mater. Sci. Eng. A* **475** 39
- [22] Chu K, Jia C, Guo H and Li W 2013 *Mater. Des.* **45** 36
- [23] Dong Z J, Li X K, Yuan G M, Cong Y, Li N, Jiang Z Y and Hu Z J 2009 *Thin Solid Films* **517** 3248
- [24] Zhang Y, Zhang H L, Wu J H and Wang X T 2011 *Scr. Mater.* **65** 1097
- [25] Pierson H O 1996 *Handbook of Refractory Carbides and Nitrides: Properties, Characteristics, Processing, and Applications* (Norwich, NJ: Noyes Publications)
- [26] Mortimer D A and Nicholas M 1973 *J. Mater. Sci.* **8** 640
- [27] Praksan K, Palaniappan S and Seshan S 1997 *Composites A* **28** 1019
- [28] Koráb J, Štefánik P, Kavecký S, Sebo P and Korb G 2002 *Composites A* **33** 133
- [29] Bouvard D *et al* 2009 *Powder Metallurgy* (London: ISTE Publishing) p 384
- [30] Pietrzak K *et al* 2017 *Arch. Metall. Mater.* **2B** 1307
- [31] Sundaram R M, Sekiguchi A, Sekiya M, Yamada T and Hata K 2018 *R. Soc. Open Sci.* **5** 180814
- [32] Zhang W, Hu Y, Pan J, Zhang J, Cui J, Yan Q and Ren S 2019 *Nanotechnology* **30** 185701
- [33] Zain-ul-abdein M, Ijaz H, Saleem W, Raza K, Mahfouz A and Mabrouki T 2017 *Materials* **10** 739
- [34] Zhang C, Cai Z, Tang Y, Wang R, Peng C and Feng Y 2018 *Diam. Relat. Mater.* **86** 98
- [35] Wang L, Li J, Che Z, Wang X, Zhang H, Wang J and Kim M 2018 *J. Alloys Compd.* **749** 1098
- [36] Chang G, Sun F, Duan J, Che Z, Wang X, Wang J, Kim M J and Zhang H 2018 *Acta Mater.* **160** 235
- [37] Cho H J, Yan D, Tam J and Erb U 2019 *J. Alloys Compd.* **791** 1128

- [38] Bai G, Wang L, Zhang Y, Wang X, Wang J, Kim M J and Zhang H 2019 *Mater. Charact.* **152** 265
- [39] Pietrzak K *et al* 2016 *J. Mater. Eng. Perform.* **25** 3077
- [40] Nayan N, Shukla A K, Chandran P, Rao Bakshi S, Murty S V S N, Pant B and Venkitakrishnan P V 2017 *Mater. Sci. Eng. A* **682** 229
- [41] Liu D, Tian H, Lin L and Shi W 2019 *Diam. Relat. Mater.* **91** 138
- [42] Hanada K, Matsuzaki K and Sano T 2004 *J. Mater. Process. Technol.* **153** 514
- [43] Abyzov A M, Kidalov S V and Shakhov F M 2012 *App. Therm. Eng.* **48** 72
- [44] Wu J, Zhang H, Zhang Y, Li J and Wang X 2012 *Mater. Des.* **39** 87
- [45] Weber L and Tavangar R 2007 *Scr. Mater.* **57** 988
- [46] Schubert T, Ciupinski L, Morgiel J, Weissmuller H, Weissgarber T and Kieback B 2007 *Proc. European Powder Metallurgy Conf.* p 319
- [47] Schubert T, Ciupinski L, Zielinski W, Michalski A, Weissgarber T and Kieback B 2008 *Scr. Mater.* **58** 263
- [48] Schubert T, Trindade B, Weissgarber T and Kieback B 2008 *Mater. Sci. Eng. A* **475** 39
- [49] Xia Y, Song Y Q, Lin C G, Cui S and Fang Z Z 2009 *Trans. Nonferrous Met. Soc. China* **19** 1161
- [50] Chu K, Liu Z F, Jia C C, Chen H, Liang X B, Gao W J, Tian W H and Guo H 2010 *J. Alloys Compd.* **490** 453
- [51] Rosinski M, Ciupinski L, Grzonka J, Michalski A and Kurzydowski K J 2012 *Diam. Relat. Mater.* **27** 29
- [52] Chu K, Jia C C, Guo H and Li W S 2013 *Mater. Des.* **45** 36
- [53] Zhang Y, Zhang H L, Wu J H and Wang X T 2011 *Scr. Mater.* **65** 1097
- [54] Dong Y H, Zhang R Q, He X B, Ye Z G and Qu X H 2012 *Mater. Sci. Eng. B* **177** 1524
- [55] Mizuuchi K *et al* 2010 *Mater. Sci. Forum* **638** 2115
- [56] Guillemet T 2013 *PhD Thesis* University of Bordeaux (France), University Nebraska Lincoln (USA)
- [57] Massalski T B 1990 *Binary Alloy Phase Diagrams* 2nd edn (Materials Park, OH: ASM International)
- [58] Veillere A, Heintz J-M, Chandra N, Douin J, Lahaye M, Lalet G, Vincent C and Silvain J-F 2011 *Mater. Res. Bull.* **47** 375
- [59] Couillaud S, Lu Y F and Silvain J-F 2014 *J. Mater. Sci.* **49** 5537
- [60] Hologado M J, Rives V and San Roman S 1992 *J. Mater. Sci. Lett.* **11** 1708
- [61] Ghosh-Dastidar A, Mahuli S, Agnihotri R and Fan L-S 1995 *Chem. Eng. Sci.* **50** 2029
- [62] Silvain J-F, Bihr J-C, Lambert J, Alnot M and Ehrhardt J J 1995 *J. Vac. Sci. Technol. A* **13** 1893
- [63] Silvain J-F, Vincent C, Heintz J-M and Chandra N 2009 *Comput. Sci. Technol.* **69** 2474
- [64] Kiflawick I and Schlesinger M 1983 *J. Electrochem. Soc.* **130** 872
- [65] Silvain J-F and Fouassier O 2004 *Surf. Interface Anal.* **36** 769
- [66] Natividad E, Heintz J-M and Silvain J-F 2004 *Surf. Sci.* **557** 129
- [67] Silvain J-F, Richard P, Douin J, Lahaye M and Heintz J-M 2007 *Mater. Sci. Forum* **534** 1445
- [68] Silvain J-F, Vincent C, Guillement T, Veillere A and Heintz J-M 2012 *Mater. Res. Bull.* **47** 500
- [69] Jiang X, Herricks T and Xia Y 2002 *Nano Lett.* **2** 1333–8
- [70] Guillement T, Heintz J-M, Mortaigne B, Lu Y and Silvain J-F 2018 *Adv. Eng. Mater.* **20** 1700894
- [71] Azina C, Roger J, Joulain A, Mauchamp V, Mortaigne B, Lu Y and Silvain J-F 2018 *J. Alloys Compd.* **738** 292
- [72] Hamilton R L and Crosser O K 1962 *Ind. Eng. Chem. Fundam.* **1** 187
- [73] Arnaud D, Barbery J, Biais R, Fargette B and Naudot P 2008 *Tech. Ing.* **M4640** 1
- [74] Roosen A 1998 *Ceram. Trans.* **1** 675
- [75] Geffroy P-M, Chartier T and Silvain J-F 2007 *J. Eur. Ceram. Soc.* **27** 291
- [76] Guillement T, Geffroy P-M, Heintz J-M, Chandra N, Lu Y and Silvain J-F 2012 *Composites A* **43** 1746
- [77] Jiang X, Herricks T and Xia Y 2002 *Nano Lett.* **2** 1333
- [78] Ekimov E A, Suetin N V, Popovitch A F and Ralchenko V G 2008 *Diam. Relat. Mater.* **17** 838